JOURNAL OF AIRCRAFT
Vol. 44, No. 5, September–October 2007

Nonlinear Flight Dynamics of Very Flexible Aircraft

Christopher M. Shearer* and Carlos E. S. Cesnik†
University of Michigan, Ann Arbor, Michigan 48109

DOI: 10.2514/1.27606

This paper focuses on the characterization of the response of a very flexible aircraft in flight. The six-degree-of-freedom equations of motion of a reference point on the aircraft are coupled with the aeroelastic equations that govern the geometrically nonlinear structural response of the vehicle. A low-order strain-based nonlinear structural analysis coupled with unsteady finite state potential-flow aerodynamics form the basis for the aeroelastic model. The nonlinear beam structural model assumes constant strain over an element in extension, twist, and in/out-of-plane bending. The geometrically nonlinear structural formulation, the finite state aerodynamic model, and the nonlinear rigid-body equations together provide a low-order complete nonlinear aircraft analysis tool. The equations of motion are integrated using an implicit modified Newmark method. The method incorporates both first- and second-order nonlinear equations without the necessity of transforming the equations to first order and incorporates a Newton–Raphson subiteration scheme at each time step. Using the developed tool, analyses and simulations can be conducted that encompass nonlinear rigid-body, nonlinear rigid-body coupled with linearized structural solutions, and full nonlinear rigid-body and structural solutions. Simulations are presented that highlight the importance of nonlinear structural modeling compared with rigid-body and linearized structural analyses in a representative high-altitude long-endurance vehicle. Results show significant differences in the three reference point axes (pitch, roll, and yaw) not previously captured by linearized or rigid-body approaches. The simulations using both full and empty fuel states include level gliding descent, low-pass-filtered square aileron, input rolling/gliding descent, and low-pass square elevator input gliding descent. Results are compared for rigid-body, linearized structural, and nonlinear structural response.

Nomenclature

A	=	cross-sectional area
B	=	fixed-body reference frame
b	=	displacements and rotations as time integral of β; semichord length
C^{GB}	=	rotation matrix from the B and G frames
c_{ij}	=	direction cosine between elements i and j
cm	=	center of mass
D_{ij}	=	connecting matrix between elements i and j
d	=	distance from midchord to the beam reference line
$\mathbf{F}_B$	=	linear force vector applied at the B reference frame
$f(\cdot)$	=	generic function
$f_{\mathrm{dst}}, f_{\mathrm{pt}}$	=	distributed and point forces
$f_{L_{\mathrm{corr}}}$	=	tip-loss correction function
G	=	inertial frame
$\bar{G}_{(e)}$	=	spatial-dependent matrix of strains for element e
g_0	=	gravity column vector
H	=	modified Jacobian matrix
h	=	position and orientation vector of the flexible structure
I	=	identity matrix
$\mathbf{I}_B$	=	inertia dyadic with respect to the B reference frame
I_B	=	inertia matrix
J	=	Jacobian matrix
J_{trim}	=	trim cost function
K_ϵ	=	matrix of strains
$L^{\mathrm{aero}}, L^{\delta}$	=	airfoil lift force and lift force due to control surface deflection, respectively
$M^{\mathrm{aero}}, M^{\delta}$	=	airfoil pitching moment and pitching moment due to control surface deflection, respectively
m	=	mass per unit span
M, C, K	=	generalized mass, damping, and stiffness matrices
$\mathbf{M}_B$	=	moment vector applied at the B reference frame
$M_{\mathrm{dst}}, M_{\mathrm{pt}}$	=	distributed and point moments
O	=	origin of the B reference frame
p	=	position of the origin of the w frame with respect to the origin of the inertial frame
p_a	=	position of an arbitrary point in the vehicle with respect to the origin of the inertial frame
p_B	=	inertial position of the B reference frame
$\mathbf{p}_B$	=	inertial position vector of the B reference frame
p_r	=	position from the B reference frame origin to the local w reference frame
$\mathbf{p}_{r_{\mathrm{cm}}}$	=	vector from the B reference frame origin to the center of mass
q	=	generalized displacement column vector
R	=	generalized force column vector
R_B	=	generalized force applied to the B reference frame states
R_F	=	generalized force applied to elastic states
$\mathcal{S}$	=	search variable column vector
s	=	undeformed beam spatial dimension
t	=	time
v_B	=	linear velocity of the B reference frame
w	=	local elastic reference frame
w_x, w_y, w_z	=	column vectors of unit vector components of the local elastic reference frame
α	=	angle of attack
β	=	column vector of the B reference frame linear and angular velocities
δ_u	=	control surface angle deflection
ϵ	=	column vector of the elastic strain state

Presented as Paper 5805 at the Atmospheric Flight Mechanics, San Franscisco, CA, 15–18 August 2005; received 31 August 2006; revision received 6 December 2006; accepted for publication 4 January 2007.

*Major, U.S. Air Force, Ph.D. Candidate, currently Assistant Professor of Aerospace Engineering, U.S. Air Force Institute of Technology, Dayton, Ohio; christopher.shearer@afit.edu. Student Member AIAA.

†Associate Professor of Aerospace Engineering; cesnik@umich.edu. Associate Fellow AIAA.

$\epsilon_x, \kappa_x, \kappa_y, \kappa_z$	=	element strains corresponding to extension, twist, and in- and out-of-plane bending
ζ	=	quaternion column vector used for the B reference frame orientation
$\mathbf{\Theta}_B$	=	generalized B reference frame rotation vector
λ	=	column vector of inflow states
λ_0	=	inflow velocity
ρ	=	density
τ	=	user-defined tip-loss parameter
$\phi_{(e),(e-1)}$	=	discrete rotation angle between elements e and $e-1$
$\tilde{\Omega}$	=	matrix of angular velocities ω_B
$\boldsymbol{\omega}_B$	=	angular velocity vector of the B reference frame
ω_B	=	angular velocity of the B reference frame
$\tilde{(\cdot)}$	=	skew-symmetric matrix operator
$\tilde{(\cdot)}^T$	=	transpose of skew-symmetric matrix operator
$\dot{(\cdot)}$	=	derivative with respect to time
$\bar{(\cdot)}$	=	finite element discretization of the quantity $(\cdot)$

Subscripts

B	=	reference to the fixed-body reference frame
BB, BF	=	contributions of a particular matrix to the body and body/flexible differential equations of motion
bc	=	boundary condition
cm	=	center of mass
cs	=	cross-sectional quantity
d	=	wing dihedral
d'Alm	=	D'Almbert's
(e)	=	element number, elevator
end	=	end of element
ext	=	external
F	=	reference to the flexible degree of freedom
FF, FB	=	contributions of a particular matrix to the flexible/body differential equations of motion
G	=	global matrix
$h\epsilon, hb$	=	h vector with respect to strain ϵ or displacement/rotation of the B reference frame, respectively
r	=	relative, rudder
s	=	wing sweep
t	=	wing twist, thrust
u	=	control input
x, y, z	=	reference to x, y, and z directions
0	=	beginning of element
$1D$	=	per unit length
$3D$	=	per unit volume

Superscripts

aero	=	related to aerodynamic effects
k	=	member index, a member is a collection of elements
s	=	undeformed beam spatial dimension
T	=	transpose operator
*	=	reordered rows and/or columns of the entity

I. Introduction

ON 17 DECEMBER 1903, the Wright brothers set about the task of launching an airplane into the sky. Their multiple successes that day have been hailed as the start of heavier-than-air, powered flight. One of the key features of their aircraft was the use of wing flexibility for roll control. Because of the low dynamic pressure seen on that flight and the relatively high stiffness-to-mass ratio of the aircraft, the Wrights were able to develop the required control power without any detrimental aeroelastic effects. However, almost 100 years later on 26 June 2003, NASA's Helios aircraft [1]

> HP03-2 took off at 10:06 a.m. local time from the Navy Pacific Missile Range Facility (PMRF) located on the island of Kauai, Hawaii. . . . At 10:22 a.m. and 10:24 a.m., the aircraft encountered turbulence and the wing dihedral became much larger than normal and mild pitch oscillations began but quickly damped out. At about 30 min into the flight, the aircraft encountered turbulence and morphed into an unexpected, persistent, high dihedral configuration. As a result of the persistent high dihedral, the aircraft became unstable in a very divergent pitch mode in which the airspeed excursions from the nominal flight speed about doubled every cycle of the oscillation. The aircraft design airspeed was subsequently exceeded and the resulting high dynamic pressures caused the wing leading-edge secondary structure on the outer wing panels to fail and the solar cells and skin on the upper surface of the wing to rip off. The aircraft impacted the ocean within the confines of the PMRF test range and was destroyed. . . . The root causes of the mishap include: [A] lack of adequate analysis methods led to an inaccurate risk assessment of the effects of configuration changes leading to an inappropriate decision to fly an aircraft configuration highly sensitive to disturbances . . . [and] configuration changes to the aircraft, driven by programmatic and technological constraints, altered the aircraft from a spanloader to a highly point-loaded mass distribution on the same structure significantly reducing design robustness and margins of safety.

The Helios accident highlighted our limited understanding and limited analytical tools necessary for designing very flexible aircraft and to potentially exploit aircraft flexibility. The number one root cause/recommendation from NASA [1] was "[that] more advanced, multidisciplinary (structures, aeroelastic, aerodynamics, atmospheric, materials, propulsion, controls, etc.) time-domain analysis methods appropriate to highly flexible, morphing vehicles [be developed]."

Despite the lack of fundamental understanding on the behavior of these vehicles, recent advances in airborne sensors and communication packages have brought the need for high-altitude long-endurance (HALE) aircraft. These platforms can be categorized under three broad missions, supporting either the military or civilian communities. The missions include airborne intelligence, surveillance, and reconnaissance (ISR) for the military [2]; network communication nodes for the military and civilian usage; and general atmospheric research [3]. Because of the mission requirements, the desired vehicles are characterized by high-aspect-ratio wings and slender fuselages, resulting in very flexible vehicles. Examples of mission optimization studies for this class of vehicle can be found in [2], in which it is shown the aircraft are required to have a fuel fraction greater than 66%. This results in a very small structural weight fraction. The combination of high aerodynamic efficiency and low structural weight fraction yields inherently flexible wings and nonlinear structural and flight dynamics. The HALE vehicle will then be susceptible to large dynamic wing deformations at low frequencies, presenting a direct impact into the flight dynamic characteristics of the vehicle, as was seen in the Helios flight tests [1].

The mission of the HALE aircraft is planned to be unmanned due to its "dull, dirty, or dangerous" [4] nature, that is,

> the attributes that make the use of unmanned preferable to manned aircraft . . . [are] in the case of the dull, the better sustained alertness of machines over that of humans and, for the dirty and the dangerous, the lower political and human cost if the mission is lost, and greater probability that the mission will be successful. Lower downside risk and higher confidence in mission success are two strong motivators for continued expansion of unmanned aircraft systems.

For all of the reasons stated, a better understanding of the flight dynamics of these vehicles is required. This research addresses several of the key areas required to aid in understanding the flight dynamics and trajectory control of HALE aircraft; specifically, the development of nonlinear structurally coupled aeroelastic equations of motion (EOM), long-term numerical integration of the governing differential algebraic equations, and stabilizing and trajectory following control architecture. Although there are commercial software tools capable of dealing with pieces of the problem, there is no commercially available software that integrates all of the disciplines needed for such investigation as discussed here.

A. Previous Work, Coupled Flight Dynamics, and Aeroelasticity

Aircraft elastic flight dynamics have been studied and analyzed for more than three quarters of a century. However, research and applications of flexible aircraft dynamics have been based primarily on linear models or, at best, nonlinear rigid-body vehicle dynamics coupled with linear structural dynamics. For the majority of conventional aircraft, linear analysis has been very successful in providing sound aircraft designs. Recent comprehensive reviews of aeroelasticity's past, present, and future are given by Friedmann [5], Livne and Weisshaar [6], and Livne [7]. Some of the areas that Friedmann focused his review on (mid 1980s to late 1990s) were aeroservoelasticity, computational and nonlinear aeroelasticity, rotary-wing aeroelasticity, imbedded structural actuation and aeroelasticity, and the future challenges of aeroelastic research. In the area of future challenges, Friedmann pointed to the importance of the aeroservoelastic problem facing HALE-type aircraft; specifically, the "autonomous nature of these vehicles requires a high-gain control system, which will interact with flexible and rigid-body dynamics." Livne and Weishaar gave a detailed overview of the unconventional designs over the past 100 years that have invigorated the development of aeroelastic theory and tools to date. Livne then looked to the future and highlighted several of the challenges to the field of aeroelasticity.

1. *Linear Aeroelasticity*

In the past decade, several researchers have investigated different aspects of flexible aircraft structural dynamics. Researchers have typically focused on various forms of the rigid-body dynamics augmented with linear structural modeling.

Schmidt and Raney [8] developed a flexible modeling approach to be used with existing rigid-body simulations. The modeling requires aerodynamic stability derivatives, aerodynamic influence coefficients, elastic mode shapes, modal frequencies and damping, and generalized masses. The authors presented the importance of coupled flight dynamics and aeroelasticity by showing degraded Cooper–Harper pilot rating for a simulated B-1 aircraft model with both longitudinal and lateral rigid-body dynamics coupled with flexible structures. Pedro and Bigg [9] developed a simulation environment using normal mode approximation for structural modeling. The environment incorporates pilot and gust modeling so that flexibility effects can be studied on piloted aircraft response. Reschke [10] developed a full nonlinear rigid-body set of equations of motion coupled with linearized structural dynamics for the recovery of aircraft loads. Kier [11] used Reschke's work and applied different aerodynamic theories to compare load recovery and computational time. Both authors applied their work to a large transport aircraft. Crimaldi et al. [12] compared symmetric and asymmetric gust loading for load recovery for a B-2 flying wing model using linear elastic modes. Their research shows that for a flying wing aircraft, symmetric gusts provide the highest loads. Although these approaches are applicable to a wide class of high-performance flight vehicles and provide valuable insight into aeroelastic problem areas, they are not sufficient to deal with the changing mass properties and low stiffness characteristics of very flexible aircraft.

2. *Nonlinear Aeroelasticity*

Early nonlinear aeroelastic work in very flexible aircraft was conducted by van Schoor and von Flotow [13]. Their work demonstrated the critical importance of including aircraft structural dynamics when analyzing aircraft flight dynamics of very flexible aircraft. They showed, using linearized analysis about nonlinear equilibrium points, a significant change in the classic rigid-body modes when flexible structural modeling is included.

More recently, Patil et al. [14] developed a formulation for the complete modeling of a HALE-type vehicle. The formulation has been validated against the Goland wing [15]. Patil et al. [16] continued the work, showing a significant change in flight dynamic characteristics due to wing flexibility. Their work shows a significant difference between the short period and phugoid modes of a very flexible aircraft when comparing rigid-body, linear aeroelastic, and nonlinear aeroelastic dynamics. The short period and phugoid modes were obtained by linearizing the nonlinear dynamics about a nonlinear equilibrium. In a parallel effort, Drela [17] developed an integrated analysis tool for conceptual aerodynamic, structural, and control-law design of an aircraft implemented in ASWING. The code provides rapid analysis during the early phases of aircraft design. The formulation is based on geometrically nonlinear isotropic beam analysis and lifting-line aerodynamics with a one-lag term for unsteadiness corrections.

Furthering the development of nonlinear structural analysis tools, Cesnik and Brown [18,19] introduced the strain-based approach for the modeling of highly flexible aircraft. In [19], HALE aircraft were modeled using a rigid fuselage and a highly flexible high-aspect-ratio composite wing. The nonlinear structural dynamic analysis is a strain-based approach solved in the time domain, which has been validated against the Goland wing [20]. The authors studied the time-marching aeroelastic and aeroservoelastic behavior of cantilevered wings and HALE aircraft under constrained reference frame motion with imbedded actuation. For unsteady aerodynamics, the finite state two-dimensional strip theory of Peters et al. [21,22] is used. Time marching is accomplished using a trapezoidal integration scheme. Their work using the finite strain formulation and finite state aerodynamics provides the basis for the structural and aerodynamic formulation of this paper.

Cesnik and Su [23] extended the work of [19] by adding a flexible fuselage and developing a split beam formulation. The work focused on a full aircraft constrained to roll and comparing different configurations for roll performance and nonlinear flutter.

Patil and Hodges [24], Su and Cesnik [25], and Patil and Taylor [26] studied the nonlinear structural flight dynamics of a flying wing configuration using 1-D beam modeling for slender structures. All of these papers use the Peters et al. [21,22] unsteady aerodynamics model. Additionally, Su and Cesnik addressed torsional stiffness changes due to wrinkling of the skin. Wang et al. [27] studied a flying wing using the geometrically exact beam modeling coupled with an aerodynamic model using an unsteady vortex lattice method. Their work highlights the importance of including nonlinear structural dynamics for asymmetric maneuvering.

Palacios and Cesnik [28] developed nonlinear aeroelastic tools. They developed a high-fidelity modeling framework in which the flow is modeled using the 3-D Euler equations, and the 3-D structural deformation is modeled using split 1-D and 2-D framework. The 1-D structural deformation follows traditional 1-D beam theory, in which the cross section perpendicular to the beam reference line is assumed to be undeformed during bending. The 2-D framework allows for changes to the cross section based upon internal and external loading. Because of the computational size of the coupled structure/CFD solution, results have only been developed for steady-state solutions. Garcia [29] also incorporated a nonlinear finite element model coupled with the full Euler/Navier–Stokes. Garcia's results show significant difference between linear and nonlinear structural modeling for a cantilevered swept wing model.

Blair and Canfield [30] developed an integrated design process for evaluating weight estimates of the joined-wing HALE aircraft concept, incorporating the disciplines of structures, aerodynamics, and aeroelasticity. Their work focuses on weight determination given structural constraints and using nonlinear static aeroelastic formulations. Additionally, static aerodynamics were modeled using vortex lattice formulations. In a similar manner, Weishaar and Lee [31] also studied the weight effects due to high-aspect-ratio joined-wing concepts. Their research showed the importance of weight and c.g. location on the effect of body-freedom flutter.

Tang et al. [32] provided experimental validation of linear structural modeling coupled with nonlinear trailing-edge flap deflections using the finite state aerodynamic model. Results show good correlation between the theory and experimental results. Tang and Dowell [33,34] provided experimental validation of an ONERA unsteady aerodynamic model coupled with nonlinear structural modeling. They have shown good agreement between theory and experimental results for cantilevered HALE-like wings during limit-

cycle oscillations. A review of cantilevered structures with nonlinear aeroelasticity is provided by Dowell and Tang [35], in which they discuss several different types of aeroelastic nonlinearities, with a section devoted to HALE-type structures.

All of these studies have contributed in different ways toward the understanding of the nonlinear response and stability of highly flexible aircraft. However, due to its complex coupled nature, the problem is still far from being understood. For that, one needs to fully couple the six-degree-of-freedom (6-DOF) dynamics of the vehicle with its geometrically nonlinear aeroelasticity properties. As discussed previously, the mishap of NASA's Helios aircraft [1] has highlighted the importance of nonlinear analysis of very flexible aircraft. One of the key recommendations of the report was to "develop multidisciplinary (structures, aerodynamic, controls, etc.) models, which can describe the nonlinear dynamic behavior of aircraft modifications or perform incremental flight-testing." Nonlinear analysis tools are highly desirable and are certainly the first step in the development of future highly flexible vehicles.

B. Objective of the Paper

The objective of this paper is to present coupled 6-DOF vehicle dynamics with a modified version of the nonlinear strain-based structural formulation [19] for high-aspect-ratio lifting surfaces. The proposed formulation is used to analyze the differences between rigid-body, linearized aeroelastic, and nonlinear aeroelastic aircraft dynamic responses in gliding, roll-commanded, and pitch-commanded flight. This formulation will be used in the future as the basis for control design of highly flexible vehicles.

II. Theoretical Development

The development of the governing differential equations of a very flexible aircraft are presented. The resulting set of differential equations govern the geometrically nonlinear aeroelastic structural response of the vehicle. Rigid-body equations are summarized for an arbitrary B reference frame that, in general, is not located at the center of mass. A low-order strain-based nonlinear structural analysis coupled with unsteady finite state potential-flow aerodynamics form the basis for the aeroelastic model. The nonlinear beam structural model assumes constant strain over an element in extension, twist, and in/out-of-plane bending. The geometrically nonlinear structural formulation, the finite state aerodynamic model, and the nonlinear rigid-body equations together provide a low-order complete nonlinear aircraft analysis formulation.

A. Overview of Rigid-Body Coupled Aeroelastic Equations of Motion

The primary goal in any analysis of aircraft flight dynamics and control is to understand the trajectory and orientation of a fixed-body reference frame B at point O, which, in general, is not the aircraft's center of mass (Fig. 1). The means for propagating the reference frame B forward in time is done by deriving and integrating a series of first-order differential equations of the form

$$\dot{x} = f(x, u) \tag{1}$$

where x represents the states of the reference frame B, and u represents control surface and external inputs. Depending on the fidelity of the analysis, these first-order differential equations vary in their complexity, from simple linear time-invariant to nonlinear time-varying differential equations. For the classic rigid-body analysis [36], the first-order differential equations take the form

$$\begin{gathered}\dot{v}_B = f_{v_B}(v_B, \omega_B, \zeta, p_B, g_0, m, F_{\text{ext}}) \\ \dot{\omega}_B = f_{\omega_B}(\omega_B, I_B, \zeta, p_B, M_{\text{ext}}); \qquad \dot{\zeta} = f_\zeta(\omega_B, \zeta) \\ \dot{p}_B = f_{p_B}(\zeta, v_B)\end{gathered} \tag{2}$$

where the B reference frame linear and angular velocity variables are represented by v_B and ω_B; F_{ext} and M_{ext} are, in general, state-dependent external forces and moments; m is the aircraft mass; and I_B is the aircraft's inertia matrix about the origin of the B reference frame. The orientation of the B reference frame is accomplished in a variety of ways, from a minimum representation using three nonorthogonal Euler angles, to nonminimum four-parameter quaternion representation, to a nine-parameter set corresponding to the nine components of the set of unit vectors defining the triad at B. Reference [37] provides a summary of different methods used in the aerospace industry. In this paper, all three techniques are used to simplify the equations when necessary. In Eq. (2), ζ is the vector of four quaternion elements used to determine the orientation of the B reference frame. The gravitational field effects are represented by g_0.

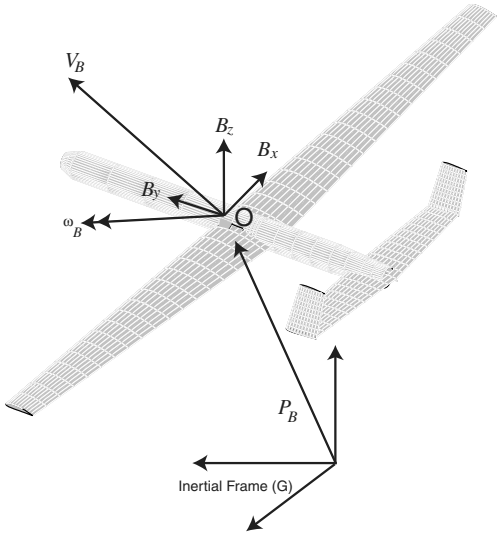

Fig. 1 Basic body reference frame and vehicle coordinates.

The classic rigid-body formulation has three key assumptions that become invalid when dealing with very flexible vehicles:

1) Inertia properties are slowly time-varying and may be assumed constant for short time simulations.

2) The coupling inertial force due to a rotating coordinate frame and relative velocity of flexible members is negligible.

3) External forces and moments, F_{ext} and M_{ext}, which come from aerodynamic loading, are based upon a fixed aircraft geometry. In the rigid-body case, Eq. (2) presents only inertial and external forces and moments. For the flexible aircraft, a set of elastic EOM is also introduced that, in the context of this study, results in

$$M\ddot{q} + C\dot{q} + Kq = (q, \dot{q}, \lambda) \tag{3}$$

$$q = \begin{Bmatrix} \epsilon \\ p_B \\ \Theta_B \end{Bmatrix}; \qquad \dot{q} = \begin{Bmatrix} \dot{\epsilon} \\ v_B \\ \omega_B \end{Bmatrix}; \qquad \ddot{q} = \begin{Bmatrix} \ddot{\epsilon} \\ \dot{v}_B \\ \dot{\omega}_B \end{Bmatrix} \tag{4}$$

where M represents generalized mass properties, q is a set of generalized coordinates containing both strain ϵ (associated with the flexible vehicle) and the inertial position p_B and an arbitrary orientation vector Θ_B of the B reference frame. The matrix C contains both structural damping and nonlinear terms associated with relative position and velocity terms associated with a rotating coordinate frame ($\omega_B \times v_B$, etc.), K is the stiffness matrix, and $R(q, \dot{q}, \lambda)$ represents generalized forces (including aerodynamic forces) that are a function of the finite state inflow λ [21,22]. Coupling of the rigid-body and flexible dynamics occurs through the dependency of M, C, and R. Typically, the B reference frame linear and angular velocities are represented by

$$\beta = \begin{Bmatrix} v_B \\ \omega_B \end{Bmatrix} \tag{5}$$

The present work uses a constant strain-based formulation [19,20] that allows for airframe nonlinear geometric deformation and accounts for geometry-dependent inertia properties of the aircraft.

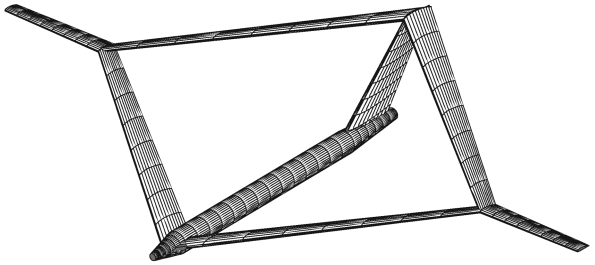

Fig. 2 Joined-wing aircraft concept.

To develop the nonlinear governing differential equations for slender elastic structures, a systematic approach is used in which the rigid body and elastic EOM are developed about the B reference frame. The differential equations for the orientation and displacement of the B reference frame are appended based upon a four-state quaternion representation. Unsteady aerodynamic modeling is included and, if required, algebraic equations for absolute or relative constraints are appended (an example of which is a joined-wing aircraft, as shown in Fig. 2, in which relative constraints are needed at the joint of the two wings).

B. Derivation of the Equations of Motion

The derivation of the EOM is based upon the principle of virtual work. The method accounts for the virtual work associated with the B reference system, flexible aircraft slender (beam) structural members, and rigid bodies attached to the flexible structures. The virtual work of a beam and rigid bodies attached to a beam are initially written in terms of dependent displacement vectors. Then the kinematic relationship between beam-dependent position vectors and the associated strains is developed. The components of virtual work are summed and the resulting set of equations is transformed from a set of dependent position vectors and a nonminimum set of B reference frame components to an independent set of strain variables and body linear and angular velocities.

1. *B Reference Frame Fuselage Contribution to the Virtual Work*

Because of the possible large deformations of the aircraft's flexible members, its center of mass is not a fixed point with respect to the fuselage. Therefore, the typical representation of the B reference frame attached to the cm becomes meaningless. Because the origin of the B frame is not taken to be the center of mass, the complete set of rigid-body EOM, which include coupling between the angular and linear velocity, must first be obtained. The complete derivation is given in [38]. To determine the rigid-body contribution to the virtual work of the entire system, a Newtonian approach based upon Greenwood [39] is used. For both the translational and rotational EOM, Fig. 3 will be used. Here, G is an inertial reference frame fixed on a flat nonrotating Earth, $\mathbf{p}_B$ is the vector from the origin of the G reference frame to the B reference frame, $\mathbf{p}_{r_{\text{cm}}}$ is from the cm of the rigid element at O (representing a piece of a rigid fuselage). Although arbitrary, the B reference frame is chosen to be at a convenient location on the elastic aircraft in which linear and angular velocities are tracked (e.g., the location of an inertial measuring unit). Elastic members are then modeled as beams that propagate from the B reference frame origin or with rigid offsets from the origin. Typically, the y axis is chosen to be tangent to the undeformed longitudinal axis of the fuselage. The x axis is chosen to be positive out of the right wing. In this way, the undeformed aircraft planform will be on a plane parallel to the x-y plane defined by the inertial frame G. Finally, the z axis is simply the cross product of the x and y axes. The final vectorial EOM have the form

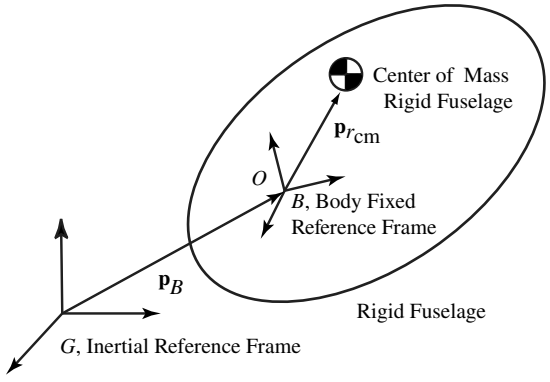

Fig. 3 Rigid-body reference frames and vectors.

$$\delta\mathbf{p}_B(m\ddot{\mathbf{p}}_B + m\ddot{\mathbf{p}}_{r_{\text{cm}}} - \mathbf{F}_B) = 0 \tag{6}$$

$$\delta\boldsymbol{\Theta}_B(\mathbf{I}_B\cdot\dot{\boldsymbol{\omega}} + \boldsymbol{\omega}_B\times\mathbf{I}_B\cdot\boldsymbol{\omega}_B + \mathbf{p}_{r_{\text{cm}}}\times m\ddot{\mathbf{p}}_B - \mathbf{M}_B) = 0 \tag{7}$$

where m is the total mass of the rigid fuselage element at O, $\mathbf{I}_B$ is the inertia dyadic about the origin of B, $\boldsymbol{\Theta}_B$ is a rotation of the B reference frame, $\mathbf{F}_B$ is the total external applied forces, and $\mathbf{M}_B$ is the total external applied moment at point O. Written in the B reference frame vector component notation, the virtual work associated with the B triad is

$$\delta W_r = \begin{Bmatrix}\delta p_B\\ \delta\Theta_B\end{Bmatrix}^T\left(\begin{bmatrix} m & m\tilde{\tilde{p}}_{r_{\text{cm}}}\\ m\tilde{\tilde{p}}^T_{r_{\text{cm}}} & I_B\end{bmatrix}\begin{Bmatrix}\dot{v}_B\\ \dot{\omega}_B\end{Bmatrix} + \begin{bmatrix} m\tilde{\omega}_B & m\tilde{\omega}_B\tilde{\tilde{p}}_{r_{\text{cm}}}\\ m\tilde{p}_{r_{\text{cm}}}\tilde{\omega}_B & \tilde{\omega}_B I_B\end{bmatrix}\begin{Bmatrix}v_B\\ \omega_B\end{Bmatrix} - \begin{Bmatrix}F_B\\ M_B\end{Bmatrix}\right) \tag{8}$$

where the operator $\tilde{(\cdot)}$ is the skew-symmetric matrix, such that if $a \equiv [\,a_1 \quad a_2 \quad a_3\,]^T$, then

$$\tilde{a} \equiv \begin{bmatrix} 0 & -a_3 & a_2\\ a_3 & 0 & -a_1\\ -a_2 & a_1 & 0\end{bmatrix} \tag{9}$$

and $\tilde{\tilde{(\cdot)}}$ is the transpose or negative of $\tilde{(\cdot)}$, such that

$$\tilde{\tilde{a}} \equiv \begin{bmatrix} 0 & a_3 & -a_2\\ -a_3 & 0 & a_1\\ a_2 & -a_1 & 0\end{bmatrix} \tag{10}$$

2. *Flexible Slender Structure Contribution to the Virtual Work*

To develop the flexible EOM, an arbitrary point in the flexible body is defined as

$$p_a = p + xw_x + yw_y + zw_z \tag{11}$$

and

$$p = p_B + p_r \tag{12}$$

where p_r is the vector from the B reference frame to a local reference frame w, and the constant scalars x, y, and z are values along the corresponding w frame orthogonal vectors w_x, w_y, and w_z, as illustrated in Fig. 4. All of the vectors are written in terms of the B reference frame. The first and second time derivatives of p_a can be written as

$$\dot{p}_a = \dot{p}_B + \dot{p}_r + x\dot{w}_x + y\dot{w}_y + z\dot{w}_z + \tilde{\omega}_B(p_r + xw_x + yw_y + zw_z) \tag{13}$$

and

$$\ddot{p}_a = \ddot{p}_B + (\ddot{p}_r + x\ddot{w}_x + y\ddot{w}_y + z\ddot{w}_z) + \dot{\tilde{\omega}}_B(p_r + xw_x + yw_y + zw_z) + 2\tilde{\omega}_B(\dot{p}_r + x\dot{w}_x + y\dot{w}_y + z\dot{w}_z) + \tilde{\omega}_B[\dot{p}_B + \tilde{\omega}_B(p_r + xw_x + yw_y + zw_z)] \tag{14}$$

Using the commutative property of the $\tilde{(\cdot)}$ operator, Eq. (14) can be

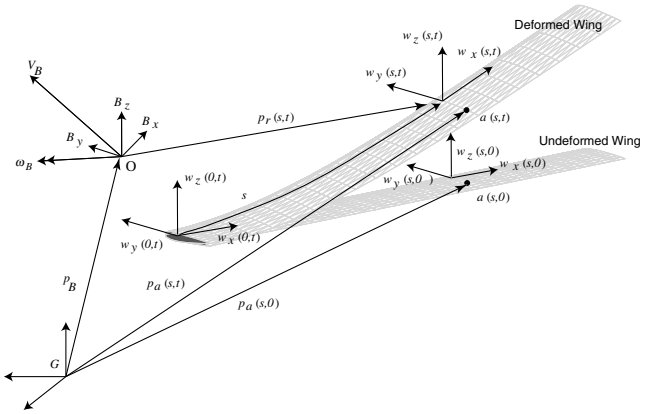

Fig. 4 Basic body reference frame and vehicle coordinates.

rewritten as

$$\ddot{p}_a = \ddot{p}_B + (\tilde{\ddot{p}}_r + x\tilde{\ddot{w}}_x + y\tilde{\ddot{w}}_y + z\tilde{\ddot{w}}_z)\dot{\omega}_B + (\ddot{p}_r + x\ddot{w}_x + y\ddot{w}_y + z\ddot{w}_z) + 2(\dot{\tilde{p}}_r + x\dot{\tilde{w}}_x + y\dot{\tilde{w}}_y + z\dot{\tilde{w}}_z)\omega_B + \tilde{\omega}_B[\dot{p}_B + (\tilde{\dot{p}}_r + x\tilde{\dot{w}}_x + y\tilde{\dot{w}}_y + z\tilde{\dot{w}}_z)\omega_B] \tag{15}$$

Using d'Almbert's principle, the inertial force per unit volume is

$$dF_{\text{d'Alm}} = -\rho\ddot{p}_a dA ds \tag{16}$$

where ρ is the volumetric density, dA is the elemental area, and ds is the elemental length along the scalar arc length s (Fig. 4). Then the virtual work per unit volume δW_{3D} and its associated virtual displacements are

$$\delta W_{3D} = -\delta p_a^T \rho \ddot{p}_a \tag{17}$$

where

$$\delta p_a \equiv \begin{bmatrix} \delta p^T & x\delta^T w_x^T & y\delta^T w_y^T & z\delta^T w_z^T \end{bmatrix}^T \tag{18}$$

and ρ is considered to be prescribed over the elemental area and length. Integrating Eq. (17) over the cross-sectional area dA and defining the cross-sectional mass matrix,

$$M_{\text{cs}} = \int_A \rho \begin{bmatrix} 1 & x & y & z \\ x & x^2 & xy & xz \\ y & xy & y^2 & yz \\ z & xz & yz & z^2 \end{bmatrix} dA \tag{19}$$

where δp^T, $\tilde{\omega}_B$, and $\tilde{(\cdot)}$ are independent of dA, the virtual work per unit length δW_{1D} is written as

$$\begin{aligned} \delta W_{1D} = -\Bigg\{ & \delta p_a^T M_{\text{cs}} \begin{bmatrix} I & \tilde{\ddot{p}}_r \\ 0 & \tilde{\ddot{w}}_x \\ 0 & \tilde{\ddot{w}}_y \\ 0 & \tilde{\ddot{w}}_z \end{bmatrix} \dot{\beta} + \delta p_a^T M_{\text{cs}} \begin{bmatrix} \ddot{p} \\ \ddot{w}_x \\ \ddot{w}_y \\ \ddot{w}_z \end{bmatrix} \\ & + 2\delta p_a^T M_{\text{cs}} \begin{bmatrix} 0 & \dot{\tilde{p}}_r \\ 0 & \dot{\tilde{w}}_x \\ 0 & \dot{\tilde{w}}_y \\ 0 & \dot{\tilde{w}}_z \end{bmatrix} \beta \\ & + \delta p_a^T M_{\text{cs}} \begin{bmatrix} \tilde{\omega}_B & 0 & 0 & 0 \\ 0 & \tilde{\omega}_B & 0 & 0 \\ 0 & 0 & \tilde{\omega}_B & 0 \\ 0 & 0 & 0 & \tilde{\omega}_B \end{bmatrix} \begin{bmatrix} I & \tilde{\dot{p}}_r \\ 0 & \tilde{\dot{w}}_x \\ 0 & \tilde{\dot{w}}_y \\ 0 & \tilde{\dot{w}}_z \end{bmatrix} \beta \Bigg\} \end{aligned} \tag{20}$$

Defining the vector h as the position and orientation at a point in the flexible body,

$$h = \begin{Bmatrix} p^T & w_x^T & w_y^T & w_z^T \end{Bmatrix}^T \tag{21}$$

which is a vector function of only ϵ and b (as shown next), then the total derivative and variation of h with respect to the independent coordinates ϵ and b are

$$\delta h = J_{h\epsilon}\delta\epsilon + J_{hb}\delta b; \qquad dh = J_{h\epsilon}d\epsilon + J_{hb}db \tag{22}$$

where

$$J_{h\epsilon} \equiv \frac{\partial h}{\partial \epsilon}; \qquad J_{hb} \equiv \frac{\partial h}{\partial b} \tag{23}$$

and $\dot{h}$ is

$$\dot{h} = J_{h\epsilon}\dot{\epsilon} + J_{hb}\dot{b} = J_{h\epsilon}\dot{\epsilon} + J_{hb}\beta \tag{24}$$

The relative velocity of h with respect to the B reference frame is $J_{h\epsilon}\dot{\epsilon}$, and the velocity of h due to the motion of the B reference frame is $J_{hb}\beta$, where

$$J_{hb} = \begin{bmatrix} I & \tilde{\tilde{p}}_r \\ 0 & \tilde{\tilde{w}}_x \\ 0 & \tilde{\tilde{w}}_y \\ 0 & \tilde{\tilde{w}}_z \end{bmatrix} \tag{25}$$

Additional Jacobians used in the formulation, along with $J_{h\epsilon}$, are derived in [38]. The relative acceleration of h due to ϵ, $\dot{\epsilon}$, and $\ddot{\epsilon}$ can be written as

$$\ddot{p}_a = \ddot{p} + x\ddot{w}_x + y\ddot{w}_y + z\ddot{w}_z = \begin{Bmatrix} 1 \\ x \\ y \\ z \end{Bmatrix}^T [\dot{J}_{h\epsilon}\dot{\epsilon} + J_{h\epsilon}\ddot{\epsilon}] \tag{26}$$

where

$$\dot{J}_{h\epsilon} = \frac{\partial (J_{h\epsilon})}{\partial \epsilon}\dot{\epsilon} \tag{27}$$

Note that $\partial(J_{h\epsilon})/\partial\epsilon$ is a three-dimensional matrix. Finally, the virtual work per unit length is

$$\begin{aligned} \delta W_{1D} = \begin{Bmatrix} \delta\epsilon \\ \delta b \end{Bmatrix}^T \Bigg(& \begin{bmatrix} J_{h\epsilon}^T M_{\text{cs}} J_{h\epsilon} & J_{h\epsilon}^T M_{\text{cs}} J_{hb} \\ J_{hb}^T M_{\text{cs}} J_{h\epsilon} & J_{hb}^T M_{\text{cs}} J_{hb} \end{bmatrix} \begin{Bmatrix} \ddot{\epsilon} \\ \ddot{\beta} \end{Bmatrix} \\ & + \begin{bmatrix} J_{h\epsilon}^T M_{\text{cs}} \dot{J}_{h\epsilon} & J_{h\epsilon}^T M_{\text{cs}} H_{hb} \\ J_{hb}^T M_{\text{cs}} \dot{J}_{h\epsilon} & J_{hb}^T M_{\text{cs}} H_{hb} \end{bmatrix} \begin{Bmatrix} \dot{\epsilon} \\ \beta \end{Bmatrix} \\ & + 2\begin{bmatrix} 0 & J_{h\epsilon}^T M_{\text{cs}} H_{h\dot{\epsilon}\dot{\beta}} \\ 0 & J_{hb}^T M_{\text{cs}} H_{hb} \end{bmatrix} \begin{Bmatrix} \dot{\epsilon} \\ \beta \end{Bmatrix} + \begin{bmatrix} C_{cs} & 0 \\ 0 & 0 \end{bmatrix} \begin{Bmatrix} \dot{\epsilon} \\ \beta \end{Bmatrix} \\ & + \begin{bmatrix} K_{cs} & 0 \\ 0 & 0 \end{bmatrix} \begin{Bmatrix} \epsilon \\ b \end{Bmatrix} - R \Bigg) \end{aligned} \tag{28}$$

where C_{cs} and K_{cs} are the generalized structural damping and stiffness matrices, respectively. Also, the following new definitions are introduced:

$$H_{h\dot{\epsilon}\dot{\beta}} \equiv \begin{bmatrix} 0 & \dot{\tilde{\tilde{p}}}_r \\ 0 & \dot{\tilde{\tilde{w}}}_x \\ 0 & \dot{\tilde{\tilde{w}}}_y \\ 0 & \dot{\tilde{\tilde{w}}}_z \end{bmatrix}; \qquad H_{hb} \equiv \tilde{\Omega} J_{hb} \tag{29}$$

$$\tilde{\Omega} \equiv \begin{bmatrix} \tilde{\omega}_B & 0 & 0 & 0 \\ 0 & \tilde{\omega}_B & 0 & 0 \\ 0 & 0 & \tilde{\omega}_B & 0 \\ 0 & 0 & 0 & \tilde{\omega}_B \end{bmatrix}$$

Note that the entries for $H_{h\dot{\epsilon}\dot{\beta}}$ come from the relative velocity of h with respect to the strain DOF:

$$J_{h\epsilon}\dot{\epsilon} = \left\{ \dot{p}_{r_x} \quad \dot{p}_{r_y} \quad \dot{p}_{r_z} \quad \dot{w}_{xx} \quad \cdots \quad \dot{w}_{zz} \right\}^T = \left\{ \dot{p}_r^T \quad \dot{w}_x^T \quad \dot{w}_y^T \quad \dot{w}_z^T \right\}^T \tag{30}$$

Before the virtual work per unit length is integrated to yield the total virtual work, the kinematic relationship and subsequent discretization of h with respect to ϵ, p_B, and the B reference frame is presented.

3. Kinematic Relationship: Constant Strain Formulation

The constant strain formulation developed by Cesnik and Brown [18,19] is adopted and summarized next. To facilitate the solution of the EOM, a spatial finite element discretization of the flexible equations is introduced here. The basic assumption is that the strain vector within a discrete beam element e, given by

$$\epsilon_{(e)}(t) = \{ \epsilon_{x(e)}(t) \quad \kappa_{x(e)}(t) \quad \kappa_{y(e)}(t) \quad \kappa_{z(e)}(t) \}^T \tag{31}$$

is spatially constant and time-dependent. The strain vector comprises the beam extension $\epsilon_{x(e)}(t)$, twist $\kappa_{x(e)}(t)$, and the two bending curvatures $\kappa_{y(e)}(t)$ and $\kappa_{z(e)}(t)$ within the element e. The gradient of the position vector h along the one-dimensional beam coordinate s is given by

$$\frac{\partial h(s,t)}{\partial s} = \bar{K}_\epsilon(s,t) h(s,t) \tag{32}$$

where

$$\bar{K}_\epsilon(s,t) = \begin{bmatrix} 0 & \bar{\varepsilon}_x(s,t) & 0 & 0 \\ 0 & 0 & \bar{\kappa}_z(s,t) & -\bar{\kappa}_y(s,t) \\ 0 & -\bar{\kappa}_z(s,t) & 0 & \bar{\kappa}_x(s,t) \\ 0 & \bar{\kappa}_y(s,t) & -\bar{\kappa}_x(s,t) & 0 \end{bmatrix} \tag{33}$$

and individual elements of $\bar{K}_\epsilon$ are 3×3 diagonal matrices, such that

$$\bar{\varepsilon}_x(s,t) = \begin{bmatrix} 1+\epsilon_x(s,t) & 0 & 0 \\ 0 & 1+\epsilon_x(s,t) & 0 \\ 0 & 0 & 1+\epsilon_x(s,t) \end{bmatrix} \tag{34}$$

$$\bar{\kappa}_z(s,t) = \begin{bmatrix} \kappa_z(s,t) & 0 & 0 \\ 0 & \kappa_z(s,t) & 0 \\ 0 & 0 & \kappa_z(s,t) \end{bmatrix} \tag{35}$$

$$\bar{\kappa}_y(s,t) = \begin{bmatrix} \kappa_y(s,t) & 0 & 0 \\ 0 & \kappa_y(s,t) & 0 \\ 0 & 0 & \kappa_y(s,t) \end{bmatrix} \tag{36}$$

and

$$\bar{\kappa}_x(s,t) = \begin{bmatrix} \kappa_x(s,t) & 0 & 0 \\ 0 & \kappa_x(s,t) & 0 \\ 0 & 0 & \kappa_x(s,t) \end{bmatrix} \tag{37}$$

Because the strain vector is assumed constant over an element, Eq. (32) is simply a spatially varying linear ordinary differential equation with constant coefficients with respect to s within the element e. Then the relation between h and ϵ can be stated as

$$h_{(e)}(s,t) = e^{(s_{(e,\text{end})} - s_{(e,0)})\bar{K}_{(e)\epsilon}} h_{(e,0)} \tag{38}$$

where $h_{(e,0)}$ is the displacement h value at $s_{(e,0)}$, the starting location along the element e. The individual components of an element position vector h are the three position components of p_r and the nine components of the element reference frame w, all expressed in the B reference system, as illustrated in Fig. 4, that is,

$$h(s,t) = \begin{bmatrix} p_{r_x} & p_{r_y} & p_{r_z} & w_{xx} & w_{xy} & w_{xz} & w_{yx} & w_{yy} & w_{yz} & w_{zx} & w_{zy} & w_{zz} \end{bmatrix}^T \tag{39}$$

Note that h is a nonminimum representation due to the nine components of the element reference frame w. This representation is chosen for convenience of the finite strain formulation.

4. Discrete Nodal Positions and the Position Vector h

In the present formulation, each element e comprises three equally spaced nodes, with corresponding position vectors $h_{(e,1)}$, $h_{(e,2)}$, and $h_{(e,3)}$, as illustrated in Fig. 5. Defining the unstrained local length of an element as $\Delta s_{(e)} = s_{(e,\text{end})} - s_{(e,0)}$ and

$$\bar{G}_{(e)} = \frac{\Delta s_{(e)}}{2} \bar{K}_{(e)\epsilon} \tag{40}$$

the kinematic relationship of the first three position vectors is

$$h_{(e,1)} = h_{(e,0)}; \qquad h_{(e,2)} = e^{\bar{G}_{(e)}} h_{(e,0)}; \qquad h_{(e,3)} = e^{2\bar{G}_{(e)}} h_{(e,0)} \tag{41}$$

5. Structural Members

A collection of contiguous elements is arranged as a member (denoted by a superscript k). It has the boundary condition defined as the position and orientation of the B reference frame (Fig. 4) or the position and orientation of the element's w reference frame of the previous member connection to this reference frame. To illustrate the concept, only members that start at point O are discussed here. Su and Cesnik [23,25] developed a split beam formulation that has been subsequently modified to have a closed-form analytical solution for h, shown next. Members are composed of an arbitrary number of key points and elements. Although Fig. 6 only illustrates a single element between each key point (KP), the formulation allows a user-defined number of elements between KPs. In general, KPs are used to distinguish slope discontinuities in the beam reference line. Additionally, the beam reference line is allowed to have a linear variation in twist between KPs, but is otherwise a straight line when unstrained.

In Fig. 6, KP1 is taken to have the boundary condition h_{bc}, that is,

$$h_{\text{bc}} = \begin{bmatrix} p_{B_x} & p_{B_y} & p_{B_z} & B_{xx} & B_{xy} & B_{xz} & B_{yx} & B_{yy} & B_{yz} & B_{zx} & B_{zy} & B_{zz} \end{bmatrix}^T \tag{42}$$

The column vector h_{bc} contains the position and orientation components of the B reference frame expressed in an inertial

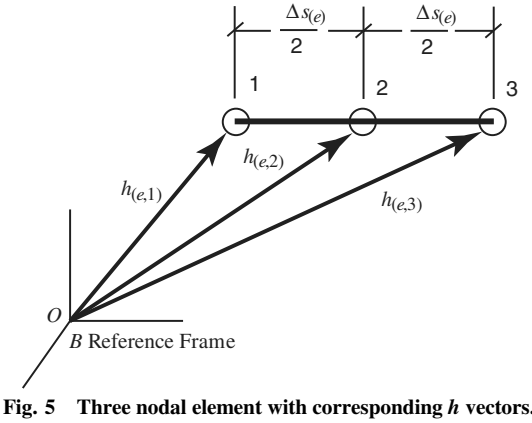

Fig. 5 Three nodal element with corresponding h vectors.

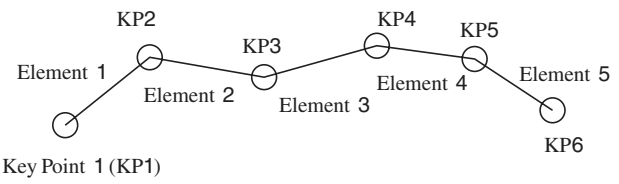

Fig. 6 Member k discretization showing key points.

coordinate system (Fig. 4). Given the arrangement in Fig. 6, the kinematic relationship between the element position and strain vectors for member k is

$$\begin{aligned} h^k_{(1,1)} &= h_{\mathrm{bc}} \\ h^k_{(1,2)} &= e^{\tilde{G}^{(k)}_1} h_{\mathrm{bc}} \\ h^k_{(1,3)} &= e^{2\tilde{G}^k_1} h_{\mathrm{bc}} \\ h^k_{(2,1)} &= D_{21} e^{2\tilde{G}^{(k)}_1} h_{\mathrm{bc}} \\ h^k_{(2,2)} &= e^{\tilde{G}^{(k)}_2} D_{21} e^{2\tilde{G}^{(k)}_1} h_{\mathrm{bc}} \\ &\vdots \\ h^k_{(2,2)} &= e^{2\tilde{G}^{(k)}_e} D^{(k)}_{(e)(e-1)} e^{2\tilde{G}^{(k)}_{(e-1)}} \cdots D^{(k)}_{21} e^{2\tilde{G}^{(k)}_1} h_{\mathrm{bc}} \end{aligned} \tag{43}$$

where $D^{(k)}_{(e)(e-1)}$ is a connecting matrix between elements e and $e-1$ and accounts for slope discontinuities. For example, D_{21}, in this case, is expressed as

$$D_{21} = \begin{bmatrix} I & 0 & 0 & 0 \\ 0 & c_{xx}I & c_{yx}I & c_{zx}I \\ 0 & c_{yx}I & c_{yy}I & c_{zy}I \\ 0 & c_{zx}I & c_{yz}I & c_{zz}I \end{bmatrix} \tag{44}$$

where c_{ij} are the direction cosines between elements 1 and 2. For example, the direction cosine matrix for a wing with twist, sweep, and dihedral is

$$\begin{aligned} c = &\begin{bmatrix} \cos\phi_{d(e),(e-1)} & 0 & \sin\phi_{d(e),(e-1)} \\ 0 & 1 & 0 \\ -\sin\phi_{d(e),(e-1)} & 0 & \cos\phi_{d(e),(e-1)} \end{bmatrix} \\ &\cdot \begin{bmatrix} \cos\phi_{s(e),(e-1)} & -\sin\phi_{s(e),(e-1)} & 0 \\ \sin\phi_{s(e),(e-1)} & \cos\phi_{s(e),(e-1)} & 0 \\ 0 & 0 & 1 \end{bmatrix} \\ &\cdot \begin{bmatrix} 1 & 0 & 0 \\ 0 & \cos\phi_{t(e),(e-1)} & -\sin\phi_{t(e),(e-1)} \\ 0 & \sin\phi_{t(e),(e-1)} & \cos\phi_{t(e),(e-1)} \end{bmatrix} \end{aligned} \tag{45}$$

where $\phi_{t(e),(e-1)}$, $\phi_{s(e),(e-1)}$, and $\phi_{d(e),(e-1)}$ are the corresponding discrete rotation angles of twist, sweep, and dihedral, respectively, between elements (e) and $(e-1)$.

6. Closed-Form Kinematic Relation

Completing the derivation of the dependent position vector h and the independent strain vector ϵ, a closed-form solution of $e^{(s-s_0)\bar{K}_\epsilon}$ is proposed here. Consider a transformation matrix T_h, so that the original h vector is reordered as h^*:

$$h^* = T_h^T h = \left\{ \left(h^*_x\right)^T \quad \left(h^*_y\right)^T \quad \left(h^*_z\right)^T \right\}^T \tag{46}$$

where

$$h^*_x = \begin{Bmatrix} p_{r_x} \\ w_{xx} \\ w_{yx} \\ w_{zx} \end{Bmatrix}; \qquad h^*_y = \begin{Bmatrix} p_{r_y} \\ w_{xy} \\ w_{yy} \\ w_{zy} \end{Bmatrix}; \qquad h^*_z = \begin{Bmatrix} p_{r_z} \\ w_{xz} \\ w_{yz} \\ w_{zz} \end{Bmatrix} \tag{47}$$

The three corresponding differential equations are

$$\frac{\partial h^*_x}{\partial s} = K_\epsilon h^*_x; \qquad \frac{\partial h^*_y}{\partial s} = K_\epsilon h^*_y; \qquad \frac{\partial h^*_z}{\partial s} = K_\epsilon h^*_z \tag{48}$$

with

$$K_\epsilon = \begin{bmatrix} 0 & 1+\epsilon_x & 0 & 0 \\ 0 & 0 & \kappa_z & -\kappa_y \\ 0 & -\kappa_z & 0 & \kappa_x \\ 0 & \kappa_y & -\kappa_x & 0 \end{bmatrix} \tag{49}$$

Using the transformation matrix T_h, $\bar{K}_\epsilon$ can be shown to be related to $\bar{K}^*_\epsilon$ by

$$\bar{K}^*_\epsilon = T_h^T \bar{K}_\epsilon T_h = \begin{bmatrix} K_\epsilon & 0 & 0 \\ 0 & K_\epsilon & 0 \\ 0 & 0 & K_\epsilon \end{bmatrix}$$

and, finally,

$$e^{(s-s_0)\bar{K}^*_\epsilon} = \begin{bmatrix} e^{(s-s_0)K_\epsilon} & 0 & 0 \\ 0 & e^{(s-s_0)K_\epsilon} & 0 \\ 0 & 0 & e^{(s-s_0)K_\epsilon} \end{bmatrix} \tag{50}$$

A closed-form solution of the terms $e^{(s-s_0)K_\epsilon}$ was derived using the Cayley–Hamilton theorem [38]. The solution is given by

$$\begin{aligned} e^{(s-s_0)K_\epsilon} = &\left(\frac{(s-s_0)}{\lambda_\kappa^2} \right. \\ &\left. - \frac{\sin[\lambda_\kappa(s-s_0)]}{\lambda_\kappa^3} \right) \begin{bmatrix} 0 & -\varepsilon_x(\kappa_z^2+\kappa_y^2) & \varepsilon_x\kappa_y\kappa_x & \varepsilon_x\kappa_z\kappa_x \\ 0 & 0 & -\kappa_z\lambda_\kappa^2 & \kappa_y\lambda_\kappa^2 \\ 0 & \kappa_z\lambda_\kappa^2 & 0 & -\kappa_x\lambda_\kappa^2 \\ 0 & -\kappa_y\lambda_\kappa^2 & \kappa_x\lambda_\kappa^2 & 0 \end{bmatrix} \\ &+ \frac{1-\cos[\lambda_\kappa(s-s_0)]}{\lambda_\kappa^2} \begin{bmatrix} 0 & 0 & \varepsilon_x\kappa_z & -\varepsilon_x\kappa_y \\ 0 & -(\lambda_\kappa^2-\kappa_x^2) & \kappa_y\kappa_x & \kappa_z\kappa_x \\ 0 & \kappa_y\kappa_x & -(\lambda_\kappa^2-\kappa_y^2) & \kappa_z\kappa_y \\ 0 & \kappa_z\kappa_x & \kappa_z\kappa_y & -(\lambda_\kappa^2-\kappa_z^2) \end{bmatrix} \\ &+ (s-s_0) \begin{bmatrix} 0 & \varepsilon_x & 0 & 0 \\ 0 & 0 & \kappa_z & -\kappa_y \\ 0 & -\kappa_z & 0 & \kappa_x \\ 0 & \kappa_y & -\kappa_x & 0 \end{bmatrix} + \begin{bmatrix} 1 & 0 & 0 & 0 \\ 0 & 1 & 0 & 0 \\ 0 & 0 & 1 & 0 \\ 0 & 0 & 0 & 1 \end{bmatrix} \end{aligned} \tag{51}$$

where

$$\lambda_\kappa = \sqrt{\kappa_x^2+\kappa_y^2+\kappa_z^2}; \qquad \varepsilon_x \equiv 1+\epsilon_x \tag{52}$$

7. Element Matrices

Using the assumption of a constant strain over an element, the matrices M_{cs}, C_{cs}, and K_{cs} are only functions of the undeformed element length Δs. The current formulation uses a three-node element for which the properties of the generalized mass, damping, and stiffness are assumed to vary linearly between nodes of an element. Using this assumption, an element mass matrix is written as

$$\begin{aligned} &M_{(e)} \\ &= \frac{1}{2}\Delta s_{(e)} \begin{bmatrix} \frac{1}{4}M_1 + \frac{1}{12}M_2 & \frac{1}{12}M_1 + \frac{1}{12}M_2 & 0 \\ \frac{1}{12}M_1 + \frac{1}{12}M_2 & \frac{1}{12}M_1 + \frac{1}{2}M_2 + \frac{1}{12}M_3 & \frac{1}{12}M_2 + \frac{1}{12}M_3 \\ 0 & \frac{1}{12}M_2 + \frac{1}{12}M_3 & \frac{1}{12}M_2 + \frac{1}{4}M_3 \end{bmatrix} \end{aligned} \tag{53}$$

where $\Delta s_{(e)}$ is the length of the element, and the subscripts 1, 2, and 3 are related to the mass properties at each nodal position. The individual generalized cross-sectional mass matrices M_1, M_2, and M_3 are of the form

$$\begin{aligned} &M_i \\ &= \begin{bmatrix} m_{\mathrm{cs}} & m_{\mathrm{cs}} r_x & m_{\mathrm{cs}} r_y & m_{\mathrm{cs}} r_z \\ m_{\mathrm{cs}} r_x & \frac{1}{2}(I_{yy}+I_{zz}-I_{xx}) & I_{xy} & I_{xz} \\ m_{\mathrm{cs}} r_y & I_{yx} & \frac{1}{2}(I_{xx}+I_{zz}-I_{yy}) & I_{yz} \\ m_{\mathrm{cs}} r_z & I_{zx} & I_{zy} & \frac{1}{2}(I_{xx}+I_{yy}-I_{zz}) \end{bmatrix} \end{aligned} \tag{54}$$

where m_{cs} is the cross-sectional mass per unit length; r_x, r_y, and r_z are the vector components of the center of mass in the local reference system w; and I_{ij} are the cross-sectional inertia properties. In a

similar manner to Eq. (53), the element structural damping $C_{(e)}$ and stiffness $K_{(e)}$ matrices are found [20].

C. *B* Reference Frame Propagation Differential Equations

Although the virtual work associated with the flexible EOM, Eq. (28), is derived using δb, the B reference frame attitude propagation is accomplished using the first-order differential quaternion equation described in [36], that is,

$$\begin{Bmatrix} \dot{\zeta}_0 \\ \dot{\zeta}_1 \\ \dot{\zeta}_2 \\ \dot{\zeta}_3 \end{Bmatrix} = -\frac{1}{2}\begin{bmatrix} 0 & \omega_{B_x} & \omega_{B_y} & \omega_{B_z} \\ -\omega_{B_x} & 0 & -\omega_{B_z} & \omega_{B_y} \\ -\omega_{B_y} & \omega_{B_z} & 0 & -\omega_{B_x} \\ -\omega_{B_z} & -\omega_{B_y} & \omega_{B_x} & 0 \end{bmatrix}\begin{Bmatrix} \zeta_0 \\ \zeta_1 \\ \zeta_2 \\ \zeta_3 \end{Bmatrix} \equiv -\frac{1}{2}\Omega_\zeta \zeta \tag{55}$$

where ω_{B_i} is the ith component of body angular velocity. The inertial velocity of the B reference frame is given by the differential equation

$$\dot{p}_B = C^{GB} v_B \tag{56}$$

The B reference frame coordinate transformation matrix C^{GB} (which transforms a vector from the B frame coordinates to the inertial coordinates, represented in terms of quaternions ζ) is given by

$$\begin{aligned} C^{GB} &= [\,B_x \quad B_y \quad B_z\,] \\ &= \begin{bmatrix} \zeta_0^2+\zeta_1^2-\zeta_2^2-\zeta_3^2 & 2(\zeta_1\zeta_2-\zeta_0\zeta_3) & 2(\zeta_1\zeta_3+\zeta_0\zeta_2) \\ 2(\zeta_1\zeta_2+\zeta_0\zeta_3) & \zeta_0^2-\zeta_1^2+\zeta_2^2-\zeta_3^2 & 2(\zeta_2\zeta_3-\zeta_0\zeta_1) \\ 2(\zeta_1\zeta_3-\zeta_0\zeta_2) & 2(\zeta_2\zeta_3+\zeta_0\zeta_1) & \zeta_0^2-\zeta_1^2-\zeta_2^2+\zeta_3^2 \end{bmatrix} \end{aligned} \tag{57}$$

where B_i is shown in Fig. 1.

D. Unsteady Aerodynamics

For this study, the unsteady aerodynamic forces and moments are calculated based upon the finite state aerodynamic theory of Peters and coworkers [21,22]. The theory is derived for a two-dimensional thin airfoil operating in inviscid and incompressible flow. The state-space form of the unsteady aerodynamic formulation makes it particularly suitable for future control studies within this framework. Although very flexible aircraft (specifically, HALE aircraft) have the potential to perform missions at high altitudes in which compressibility and Reynolds number effects are important, those effects are not considered in this work. The lift L^{aero} and the moment M^{aero} about the beam reference line, excluding contributions from trailing-edge control surfaces, are given by

$$\begin{aligned} L^{\text{aero}} &= 2\pi\rho b\left(-\dot{y}\,\dot{z} + (b-d)\dot{y}\,\dot{\alpha} - \dot{y}\lambda_0 - \tfrac{1}{2}b\ddot{z} - \tfrac{1}{2}bd\ddot{\alpha}\right) \\ M^{\text{aero}} &= dL^{\text{aero}} + 2\pi\rho b^2\left(-\tfrac{1}{2}\dot{y}\,\dot{z} - \tfrac{1}{2}d\dot{y}\,\dot{\alpha} - \frac{1}{2}\dot{y}\lambda_0 - \tfrac{1}{16}b^2\ddot{\alpha}\right) \end{aligned} \tag{58}$$

The velocity vector components are $\dot{y}$ along the chord and $\dot{z}$ perpendicular to the chord, and α is the local angle of attack. The velocity components and angle of attack are derived from the beam nodal h vector. The inflow velocity is given by

$$\lambda_0 = \frac{1}{2}\sum_{n=1}^{N} b_n \lambda_n \tag{59}$$

where the inflow states λ_n are governed by the differential equation

$$\dot{\lambda} = E_1\lambda + E_2\ddot{z} + E_3\ddot{\alpha} + E_4\dot{\alpha} \tag{60}$$

The matrices E_i are given in [21]. The b_n coefficients are binomial expansion coefficients given in Appendix C of [22]. Although λ_0 is actually an infinite sum, λ_0 can be approximated with reasonable results by letting N be between 4 and 8.

Additional aerodynamic lift L^δ and moment M^δ are generated by discrete trailing-edge surface deflections δ_u. For the two-dimensional strip theory used, the additional lift and moment are

$$L^\delta = 2\pi\rho b\left(c_1\dot{y}^2\delta_u + c_2\dot{y}\dot{\delta}_u + c_3\ddot{\delta}_u\right) \tag{61}$$

and

$$\begin{aligned} M^\delta = 2\pi\rho b[&d(c_1\dot{y}^2\delta_u + c_2\dot{y}\dot{\delta}_u + c_3\ddot{\delta}_u) + b(c_4\dot{y}^2\delta_u + c_5\dot{y}\dot{\delta}_u \\ &+ c_6\ddot{\delta}_u)] \end{aligned} \tag{62}$$

The coefficients c_1 through c_6 are based upon geometry and complete details are provided in [20,21]. In practice, the trailing-edge deflection rate terms $\dot{\delta}_u$ and $\ddot{\delta}_u$ are much smaller in magnitude than the deflection term δ_u and are neglected in this study.

To use this two-dimensional theory for a three-dimensional wing, a spanwise lift distribution function is used to correct for the tip loss and is assumed to be

$$f_{L_{\text{corr}}} = 1 - e^{-\tau s} \tag{63}$$

where τ is a user-defined input that controls the spanwise lift deficiency correction. In the final form, the generalized force, moment, and inflow equations take the form

$$F^{\text{aero}} = f(q, \dot{q}_{,0}); \qquad M^{\text{aero}} = f(q, \dot{q}_{,0}) \tag{64}$$

and

$$\dot{\lambda} = F_1\ddot{q} + F_2\dot{q} + F_3\lambda \tag{65}$$

A simplified stall model was used such that when the local angle of attack reached a user-defined angle, lift and moment generated by the airfoil was held constant. Additional lift and moments due to discrete trailing-edge surfaces were unaffected by this stall model. Further discussions on stall models and their effects on the simulation of flexible aircraft can be found in [25].

E. Complete Governing Differential Equations

Consider the relationship between the variation and differential-dependent position vector h and the independent vectors ϵ and b [Eq. (22)], the dependent velocity vector $\dot{h}$ and independent rates $\dot{\epsilon}$ and β [Eq. (24)], and the dependent acceleration vector $\ddot{h}$ and the independent rates and accelerations $\ddot{\epsilon}$ and $\dot{\beta}$ [Eq. (26)]. Summing up all of the element virtual work contributions [Eq. (28)] and the rigid-body contributions [Eq. (8)], the total virtual work can be written as

$$\begin{aligned} \delta W = [\,\delta\epsilon^T \quad \delta^T\,]^T\Bigg(&-\begin{bmatrix} M_{FF} & M_{FB} \\ M_{BF} & M_{BB} \end{bmatrix}\begin{bmatrix} \ddot{\epsilon} \\ \dot{\beta} \end{bmatrix} - \begin{bmatrix} C_{FF} & C_{FB} \\ C_{BF} & C_{BB} \end{bmatrix}\begin{bmatrix} \dot{\epsilon} \\ \beta \end{bmatrix} \\ &- \begin{bmatrix} K_{FF} & K_{FB} \\ K_{BF} & K_{BB} \end{bmatrix}\begin{bmatrix} \epsilon \\ b \end{bmatrix} + R\Bigg) \end{aligned} \tag{66}$$

where

$$\begin{aligned} &M_{FF} = J_{h\epsilon}^T M_G J_{h\epsilon}; && M_{FB} = J_{h\epsilon}^T M_G J_{hb} \\ &M_{BF} = J_{hb}^T M_G J_{h\epsilon}; && M_{BB} = J_{hb}^T M_G J_{hb} + M_B \\ &C_{FF} = J_{h\epsilon}^T M_G \dot{J}_{h\epsilon} + C_G; && C_{FB} = J_{h\epsilon}^T M_G H_{hb} + 2J_{h\epsilon}^T M_G H_{h\dot{\epsilon}\,\dot{\beta}} \\ &C_{BF} = J_{hb}^T M_G \dot{J}_{h\epsilon}; && C_{BB} = J_{hb}^T M_G H_{hb} + 2J_{hb}^T M_G H_{h\dot{\epsilon}\,\dot{\beta}} + C_B \\ &K_{FF} = K_G; && K_{FB} = 0 \\ &K_{BF} = 0; && K_{BB} = 0 \end{aligned} \tag{67}$$

and M_G, C_G, and K_G are the assembled flexible-element generalized mass, damping, and stiffness matrices, respectively, where they take the form

$$M_G = \begin{bmatrix} M_{(1)} & 0 & \cdots & 0 \\ 0 & M_{(2)} & \cdots & 0 \\ & & \ddots & \\ 0 & 0 & \cdots & M_{(e)} \end{bmatrix} \tag{68}$$

The matrices M_B and C_B represent the mass and damping matrices associated with the B frame element portion, as described in Sec. I, Eq. (8), that is,

$$M_B = \begin{bmatrix} m & m\tilde{\tilde{p}}_{r_{\text{cm}}} \\ m\tilde{p}_{r_{\text{cm}}} & I_B \end{bmatrix}; \qquad C_B = \begin{bmatrix} m\tilde{\omega}_B & m\tilde{\omega}_B\tilde{\tilde{p}}_{r_{\text{cm}}} \\ m\tilde{p}_{r_{\text{cm}}}\tilde{\omega}_B & \tilde{\omega}_B I_B \end{bmatrix} \tag{69}$$

Note the rigid-body EOM, Eq. (8), can be recovered from the flexible EOM, Eq. (66), by assuming the elastic DOF are constant. The resultant force vector R is

$$R = \begin{Bmatrix} R_F \\ R_B \end{Bmatrix} = \begin{bmatrix} K_{FF} \\ K_{BF} \end{bmatrix}\epsilon_{\text{in}} + \begin{bmatrix} B_{gF} \\ B_{gB} \end{bmatrix} g^B + \begin{bmatrix} B_{f\text{dst}F} \\ B_{f\text{dst}B} \end{bmatrix} F^{\text{dst}} + \begin{bmatrix} B_{M\text{dst}F} \\ B_{M\text{dst}B} \end{bmatrix} M^{\text{dst}} + \begin{bmatrix} B_{f\text{pt}F} \\ B_{f\text{pt}B} \end{bmatrix} F^{\text{pt}} + \begin{bmatrix} B_{M\text{pt}F} \\ B_{M\text{pt}B} \end{bmatrix} M^{\text{pt}} \tag{70}$$

where ϵ_{in} is an initial strain vector; g^B is the body-frame-B resolved gravity vector; and F^{dst}, M^{dst}, F^{pt}, and M^{pt} are body-resolved distributed and point forces and moments, respectively. The aerodynamic forces and moments, F^{aero} and M^{aero}, which are functions of control surface inputs u, are included in F^{dst} and M^{dst}. Propulsion sources (motors, propeller effects, etc.) distributed along the vehicle are contained in the terms F^{pt} and M^{pt} (e.g., [25]) The remaining component details of the resultant force vector R are given in [19].

From the principle of virtual work, Eq. (66) yields

$$\begin{bmatrix} M_{FF} & M_{FB} \\ M_{BF} & M_{BB} \end{bmatrix}\begin{Bmatrix} \ddot{\epsilon} \\ \dot{\beta} \end{Bmatrix} + \begin{bmatrix} C_{FF} & C_{FB} \\ C_{BF} & C_{BB} \end{bmatrix}\begin{Bmatrix} \dot{\epsilon} \\ \beta \end{Bmatrix} + \begin{bmatrix} K_{FF} & K_{FB} \\ K_{BF} & K_{BB} \end{bmatrix}\begin{Bmatrix} \epsilon \\ b \end{Bmatrix} = \begin{Bmatrix} R_F \\ R_B \end{Bmatrix} \tag{71}$$

This set of equations can also be written in the compact form

$$M\ddot{q} + C\dot{q} + Kq = R(q, \dot{q}, \lambda) \tag{72}$$

where the generalized mass is a function of strain, $M = f_M(\epsilon)$; the generalized damping matrix is a function of strain, strain rate, and B reference frame velocity, $C = f_C(\epsilon, \dot{\epsilon}, \beta)$; and the generalized stiffness K is constant. All of the other nonlinearities are contained in the generalized force R [Eq. (70)].

The complete set of governing differential equations is

$$\begin{aligned} M_{FF}\ddot{\epsilon} &= -M_{FB}\dot{\beta} - C_{FF}\dot{\epsilon} - C_{FB}\beta - K_{FF}\epsilon + R_F \\ M_{BB}\dot{\beta} &= -M_{BF}\ddot{\epsilon} - C_{BB}\beta - C_{BF}\dot{\epsilon} + R_B \qquad \dot{\zeta} = -\frac{1}{2}\Omega_\zeta \zeta \\ \dot{p}_B &= \begin{bmatrix} C^{BG} & 0 \end{bmatrix}\beta \qquad \dot{\lambda} = F_1\ddot{q} + F_2\dot{q} + F_3\lambda \end{aligned} \tag{73}$$

F. Trimming the Aircraft

Trimming is performed for both zero thrust and thrust required for 1-g level flight, based upon techniques outlined in [36,40]. A cost function is defined as

$$J_{\text{trim}} = f^T \cdot f \tag{74}$$

where, for the zero thrust or gliding cases,

$$f = \begin{Bmatrix} \text{pitching moment about the origin of } B \text{ frame} \\ \text{lift} - \text{weight} \end{Bmatrix} \tag{75}$$

For the case of 1-g level flight, the longitudinal B reference frame linear and angular accelerations are used, such that

$$f = \begin{Bmatrix} \dot{v}_{B_y} \\ \dot{v}_{B_z} \\ \dot{\omega}_x \end{Bmatrix} \tag{76}$$

The cost function J_{trim} is then minimized over the solution space using the elevator deflection angle δ_e, the body angle of attack α, and thrust δ_t. A simple numerical Newton–Raphson method is used to find the local minimum of the search variable, that is,

$$\Delta\mathcal{S}_k = -\left[\frac{\partial f}{\partial \mathcal{S}}\right]_k^{-1} f_k \tag{77}$$

where

$$\mathcal{S}_k = \begin{Bmatrix} \delta_e \\ \alpha \\ \delta_t \end{Bmatrix}_k \tag{78}$$

The search variable is updated by

$$\mathcal{S}_{k+1} = \mathcal{S}_k + \Delta\mathcal{S} \tag{79}$$

and f_{k+1} and $[\partial f/\partial \mathcal{S}]_{k+1}^{-1}$ are recomputed using $\mathcal{S}_{k+1}$. The process continues until the cost function J_{trim} reduces to some prescribed tolerance. To prevent divergence of the solution, $\mathcal{S}_{k+1}$ is checked at each iteration step and kept within a prescribed set of bounds. The Jacobian

$$J_f = \frac{\partial f}{\partial \mathcal{S}} \tag{80}$$

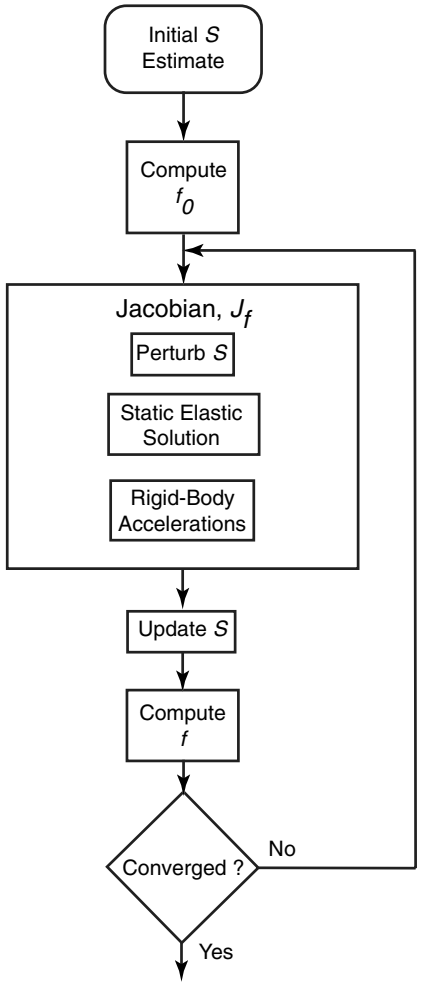

Fig. 7 Flow for trim solution.

Table 1 Geometric properties of the very flexible aircraft model

Model parameters		
Property	Value	Units
Fuselage length	26.4	m
Wing span	58.6	m
Wing area	196.3	m^2
Root chord	4.5	m
Tip chord	2.2	m
Aspect ratio	17.5	——
Wing incidence angle	3.0	deg
Horizontal tail span	18.0	m
Horizontal root chord	3.5	m
Horizontal tip chord	2.45	m
Horizontal tail incidence angle	−4.5	deg
Vertical tail span	4.0	m
Vertical root chord	2.45	m
Vertical tip chord	2.0	m
Wing/horizontal tail airfoil	NACA 4415	——
Vertical tail airfoil	NACA 0012	——
Aileron location	16.3 to 22.8	m
Aileron, elevator, rudder chord	$0.2c_{\text{local}}$	m
Aileron, elevator, rudder max/min deflections	±30	deg
Elevator span location	1.8 to 9.0	m
Rudder span location	0.8 to 3.2	m
Elements per wing	9	——
Elements per horizontal tail	5	——
Elements per vertical tail	5	——
Elements in fuselage	10	——
Total number of elements	48	——
Number of second-order states	92	——
Number of first-order states	241	——

is computed numerically through finite differences. The entire procedure is outlined in Fig. 7.

G. Solution of EOM

To solve the nonlinear differential equations (73), a high-frequency dissipative time-stepping approach was implemented based upon the second-order Newmark method. The method was modified based upon Geradin's [41] implicit integration method for time-marching integration of nonlinear second-order EOM. The resulting modified Newmark method used aspects of the generalized-α methods [42,43] and is capable of handling coupled first- and second-order nonlinear differential equations with repeated discrete eigenvalues on the unit circle. The method offers relative ease of implementation with the current EOM modeling. More details of the integration scheme can be found in [44].

III. Numerical Studies

This section presents a variety of numerical simulations that highlight the importance of using a nonlinear structural formulation for studying very flexible aircraft flight dynamics. The formulation has been implemented in the University of Michigan's nonlinear aeroelastic simulation toolbox (NAST) and it has been validated against some other published numerical and experimental results [20,38]. Although the current NAST implementation (in MATLAB) has not been optimized for maximum computer performance, reference CPU time for different simulations can be found in [44].

A. Representative HALE Aircraft

A representative HALE-type aircraft was created and is shown in Fig. 8. The relevant physical properties are summarized in Table 1. The vehicle was designed to be statically stable for moderate wing deflections in both the longitudinal and lateral axes. Table 2 also includes the trimmed longitudinal controls and state (elevator angle, thrust level, and angle of attack) for both gliding and 1-g level flights. Additional details of the vehicle's mass, structural damping, and stiffness parameters are provided in [38].

The vehicle is a conventional wing/body/tail configuration with twin vertical tails. It is representative of a HALE aircraft concept being considered by the U.S. Air Force. The aircraft has the conventional control surfaces of elevator, aileron, and twin rudders. The elevator is such that a positive elevator control input δ_e results in a negative pitching moment (nose down). The left and right ailerons have a −1:1 gearing ratio, such that a positive aileron control input δ_a results in a roll to the left (left wing down). The twin rudders have a 1:1 gear ratio, such that a positive rudder control input δ_r produces a positive yawing moment (nose left). Recall that the B reference frame orientation is x positive out of the right wing, y positive out of the nose, and z positive up. Thrust is accomplished using a simple point force applied at the origin of the B reference frame and in the y direction, such that a positive thrust input δ_t results in an acceleration in the positive y direction.

B. Rigid Aircraft, Linearized Structure, and Nonlinear Structure Open-Loop Studies

Five different case studies are presented that highlight the importance of nonlinear coupled aeroelastic/flight dynamic modeling of HALE aircraft. For each case study, three different simulations are presented, corresponding to three different solutions of Eq. (73). The first is a reduced-order solution in which all elastic DOF are removed after the vehicle comes to a steady-state deflection (rigid body with deformed structure and associated mass). The second is a linearized solution that retains the elastic DOF, but only

Table 2 Control and aircraft states and inertia properties of the very flexible aircraft model[a]

Model parameters					
Property	Value				Units
	Light, no thrust	Heavy, no thrust	Light, thrust for level flight	Heavy, thrust for level flight	
Elevator deflec angle δ_e	4.51	−16.80	−6.89	−13.68	deg
Thrust req δ_t	0	0	3.21×10^4	1.12×10^5	N
Aircraft angle of attack α	0.80	7.62	1.93	7.30	deg
Fuel mass	0	32,000	0	32,000	kg
Total mass	2.10×10^4	5.38×10^4	$2.10 \cdot 10^4$	5.38×10^4	kg
Fuel fraction	0.0	59.5	0.0	59.5	%
I^{ss}_{xx}[b]	1.48×10^6	1.75×10^6	1.49×10^6	1.75×10^6	$kg \cdot m^2$
I^{ss}_{yy}	8.20×10^5	2.93×10^6	8.19×10^5	2.93×10^6	$kg \cdot m^2$
I^{ss}_{zz}	2.27×10^6	4.46×10^6	2.26×10^6	4.47×10^6	$kg \cdot m^2$
I^{ss}_{xy}	0	0	0	0	$kg \cdot m^2$
I^{ss}_{xz}	0	0	0	0	$kg \cdot m^2$
I^{ss}_{yz}	1.82×10^4	9.20×10^4	2.06×10^4	9.00×10^4	$kg \cdot m^2$
x_{cm}	0	0	0	0	m
y_{cm}	3.13	4.33×10^{-3}	3.14	5.64×10^{-3}	m
z_{cm}	0.29	0.79	0.34	0.77	m

[a]All aircraft simulations are begun at sea level conditions and 65 m/s level flight.
[b]I^{ss} are the inertia properties in a deformed steady-state configuration.

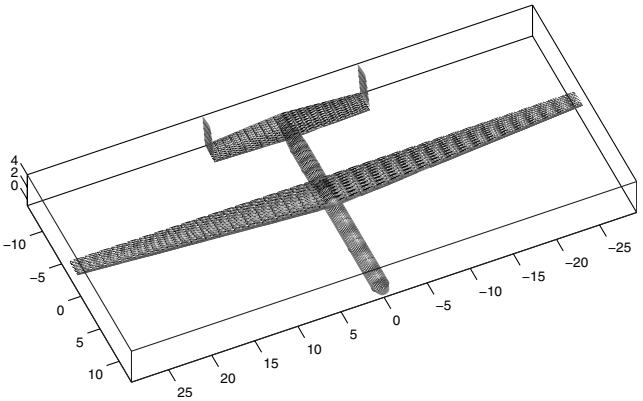

Fig. 8 Representative HALE aircraft model (units are in meters).

uses the Jacobian matrices ($J_{h\epsilon}$, J_{hb}, etc.) obtained from the steady-state solution. The third is a full nonlinear solution, starting from the steady-state deflection. The Jacobian matrices are updated at each subiteration, resulting in a full time-marching simulation of Eq. (73).

The case studies are presented at both heavy- and lightweight-fuel configurations. Three of the cases (cases 1–3) were with no thrust, and two additional cases (cases 4 and 5) were simulated with thrust required for level flight. In all cases, the only elements chosen to be flexible were the wings. The remaining body and tail elements were considered to be rigid. Case 1 is a simple straight-ahead gliding flight. Case 2 is descending flight, and case 4 is 1-g level flight. Both cases are excited with a simple modified cosine elevator input, as shown in Fig. 9, to further excite the low elastic frequency modes. Cases 3 (gliding) and 5 (1-g level flight) have a modified cosine aileron input, as shown in Fig. 10a, and a simple rudder command to alleviate the adverse yaw due to aileron input, as shown in Fig. 10b. The aileron input was chosen to achieve a maximum of approximately 45 deg of bank using the rigid aircraft model. The rudder was determined using a heuristic approach to minimize the associated yaw rate. All five cases were simulated for 30 s with a constant time step of 0.005 s.

1. *Case 1, No Thrust, Gliding Flight*

For case 1, Figs. 11 and 12 show the relevant body linear and angular velocities, v_B and ω_B. In both figures, the beginning of the classic phugoid mode can be observed, as indicated by the relatively large excursions in longitudinal velocity and small excursions in vertical velocity. For the heavy weight condition, the short period mode is seen as high-frequency oscillations, as depicted in Figs. 11b and 11c. As expected in traditional short period mode responses, the light weight configuration increases frequency and damping, hence smaller oscillations are observed in Figs. 12b and 12c. In both the heavy and light weight conditions for this vehicle, little difference is seen between the linearized and nonlinear solutions.

2. *Case 2, No Thrust, Elevator Input*

For case 2, similar results to case 1 are shown in Figs. 13 and 14. Larger variations in the body states are the main difference between the two cases. This is due to the elevator input, as defined in Fig. 9, exciting low-frequency structural modes. There are small variations between the linearized and nonlinear solutions, but the linearized solution essentially captures well the B reference frame dynamics during symmetric loading and maneuvering for the first 18 s. This is because the dominant changes associated with the generalized mass matrix (inertia about the longitudinal axis) do not couple strongly with symmetric loading and maneuvering. A weak coupling is evident at 22.3 s, in which a maximum difference of 0.27 m/s occurs in the vertical velocity. This relatively small difference (less than 3%) is attributed to the weak coupling of the nonlinear structural inertial effects and rigid-body motion. These effects are illustrated by examining the vertical wing tip position z and a difference between the linear and nonlinear solutions ($\Delta z = z_{\text{lin}} - z_{\text{non}}$), as shown in Fig. 15. Overall, this is a very particular and restrictive case for any aircraft to perform any realistic mission. Therefore, asymmetric

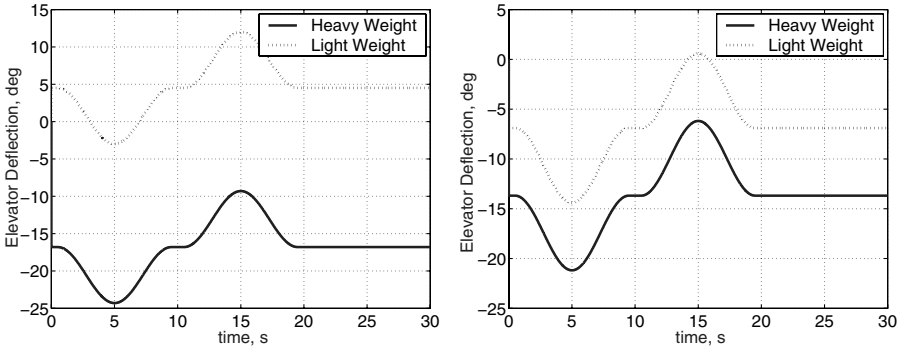

a) Case 2 **b) Case 4**

Fig. 9 Elevator control inputs for cases 2 (no thrust) and 4 (with thrust), heavy and light conditions.

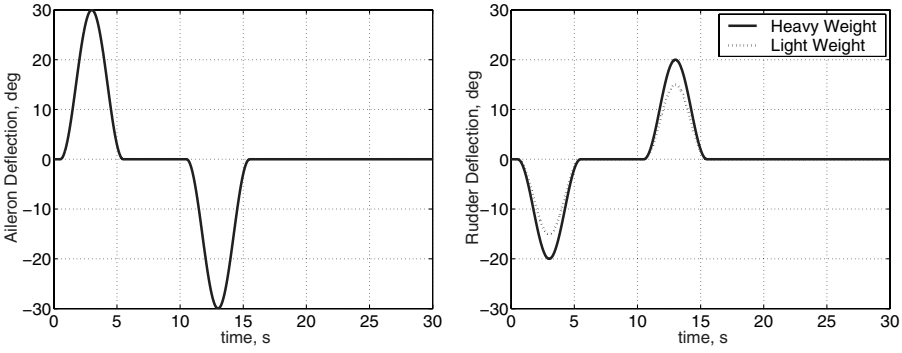

a) Aileron **b) Rudder**

Fig. 10 Lateral control inputs for cases 3 (no thrust) and 5 (with thrust), heavy and light conditions.

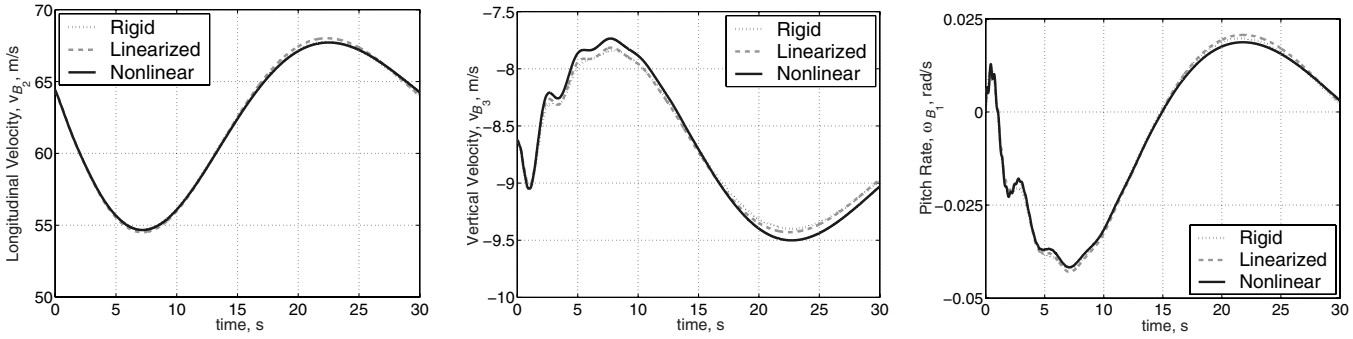

a) Longitudinal velocity b) Vertical velocity c) Pitch rate

Fig. 11 *B* reference frame relevant linear and angular rates; case 1, heavy.

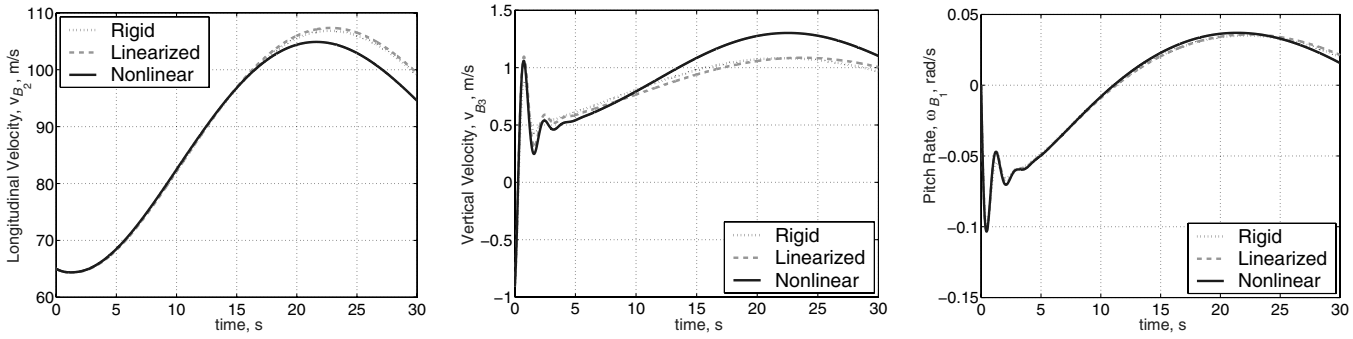

a) Longitudinal velocity b) Vertical velocity c) Pitch rate

Fig. 12 *B* Reference frame relevant linear and angular rates; case 1, light.

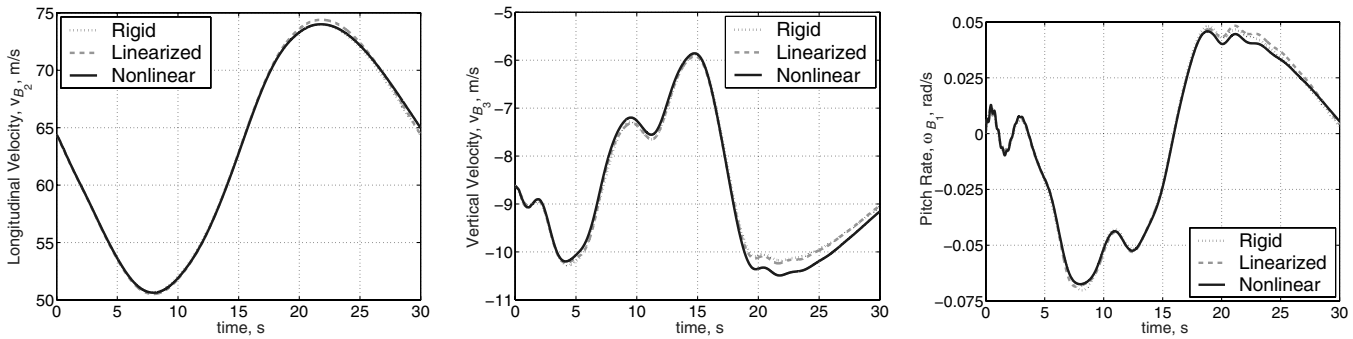

a) Longitudinal velocity b) Vertical velocity c) Pitch rate

Fig. 13 *B* reference frame relevant linear and angular rates; case 2, heavy.

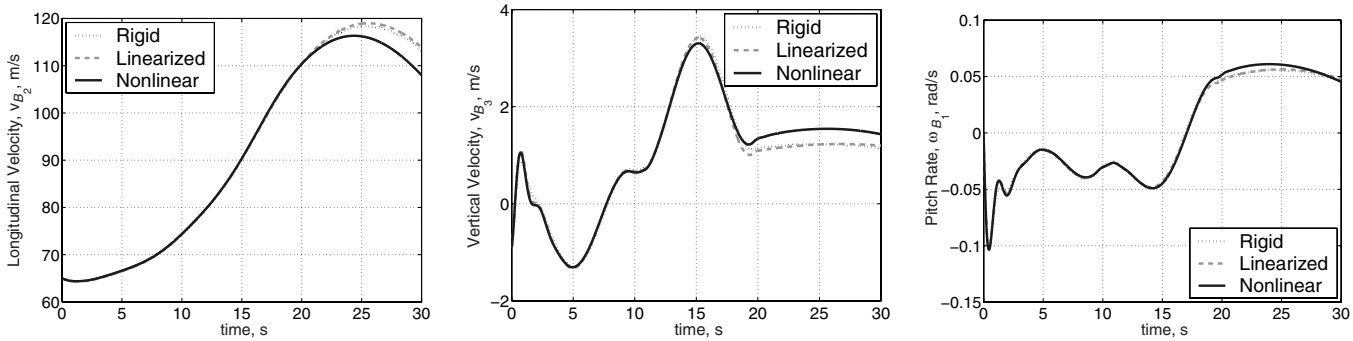

a) Longitudinal velocity b) Vertical velocity c) Pitch rate

Fig. 14 *B* reference frame relevant linear and angular rates; case 2, light.

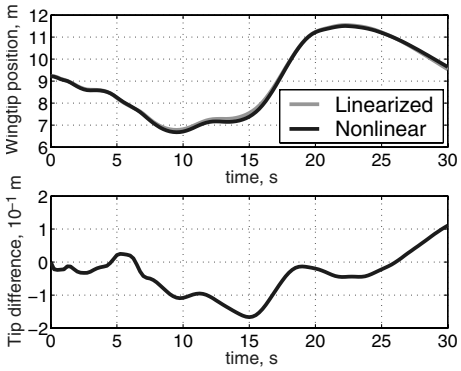

Fig. 15 Linear and nonlinear wingtip positions and their difference.

maneuvers must also be considered, in which the nonlinear structural dynamics will have a greater impact on lateral motion.

3. Case 3, No Thrust, Aileron and Rudder Input

Case 3 addresses the asymmetric loading (aileron and rudder input, as defined in Fig. 10). Results for this case are shown in Figs. 16 and 17 for heavy and light conditions, respectively. For the heavy weight condition, Fig. 16, significant differences among the three modeling approaches can be seen. The inertia effects tend to accentuate the geometrically nonlinear effects, damping out large structural motion. Mathematically, the dominant changes in the generalized mass matrix couple with the *B* reference frame dynamics. For the light weight condition, Fig. 17, a relatively high stiffness-to-mass ratio (a low fuel fraction and light weight) exists, and there is little difference between the nonlinear and linearized solutions over the first 10 s. However, geometric nonlinear effects once again start to cause significant differences in the *B* reference frame states. To further highlight the differences in the orientation of the vehicle between the formulations, the classic Euler angles are recovered and presented in Figs. 18 and 19. As one can see, the lateral yaw and roll-angle differences are significant, because Euler yaw-angle differences greater than 26 and 35 deg occur within the 30 s for the light and heavy weight conditions. Roll-angle differences of 13 and 15 deg are also experienced in the same time window. More important than the actual magnitude of the difference is the difference in sign of the roll angle in the heavy weight case (Fig. 19c). These lateral motion angles emphasize the importance of the nonlinear structural modeling. In the longitudinal axis, Euler pitch angle differences are much smaller (maximum of 3 and 5 deg). This is consistent with earlier longitudinal results.

4. Case 4, Thrust, Elevator Input

For case 4 (elevator input with thrust for level flight), results similar to case 2 are shown in Figs. 20 and 21. There are no significant differences between the rigid-body, linearized, and nonlinear simulations for the first 18 s. However, after that time the weak nonlinear coupling generates a maximum difference of 2.2% in the vertical velocity, heavy weight condition (Fig. 20b).

5. Case 5, Thrust, Aileron and Rudder Input

Similar to case 3, case 5 deals with asymmetric loading except with the addition of thrust required for level flight. Results are seen in Figs. 22 and 23. Results are similar to case 3 in that more significant differences can be seen than the elevator only input of case 4.

As in case 3, the differences are highlighted through the recovery of the classic Euler angles (Figs. 24 and 25). Here, smaller Euler-angle excursions between solutions are seen, compared with case 3. For example, in case 3, the maximum Euler-yaw-angle difference for the light weight condition was 26 deg, compared with 9 deg. Similar reductions in roll-angle differences are also seen. These reductions in lateral motion differences are due to the addition of thrust required to overcome drag in level flight. This results in smaller-magnitude excursions of the longitudinal velocities, which have a direct impact on aerodynamic rolling moment. Despite the reduced Euler-angle differences compared with case 3, the magnitude of the differences is still significant, requiring nonlinear structural analysis.

IV. Conclusions

A framework for analyzing the flight dynamics of very flexible vehicle configurations typically used in HALE aircraft was presented. It tightly couples the nonlinear 6-DOF equations of

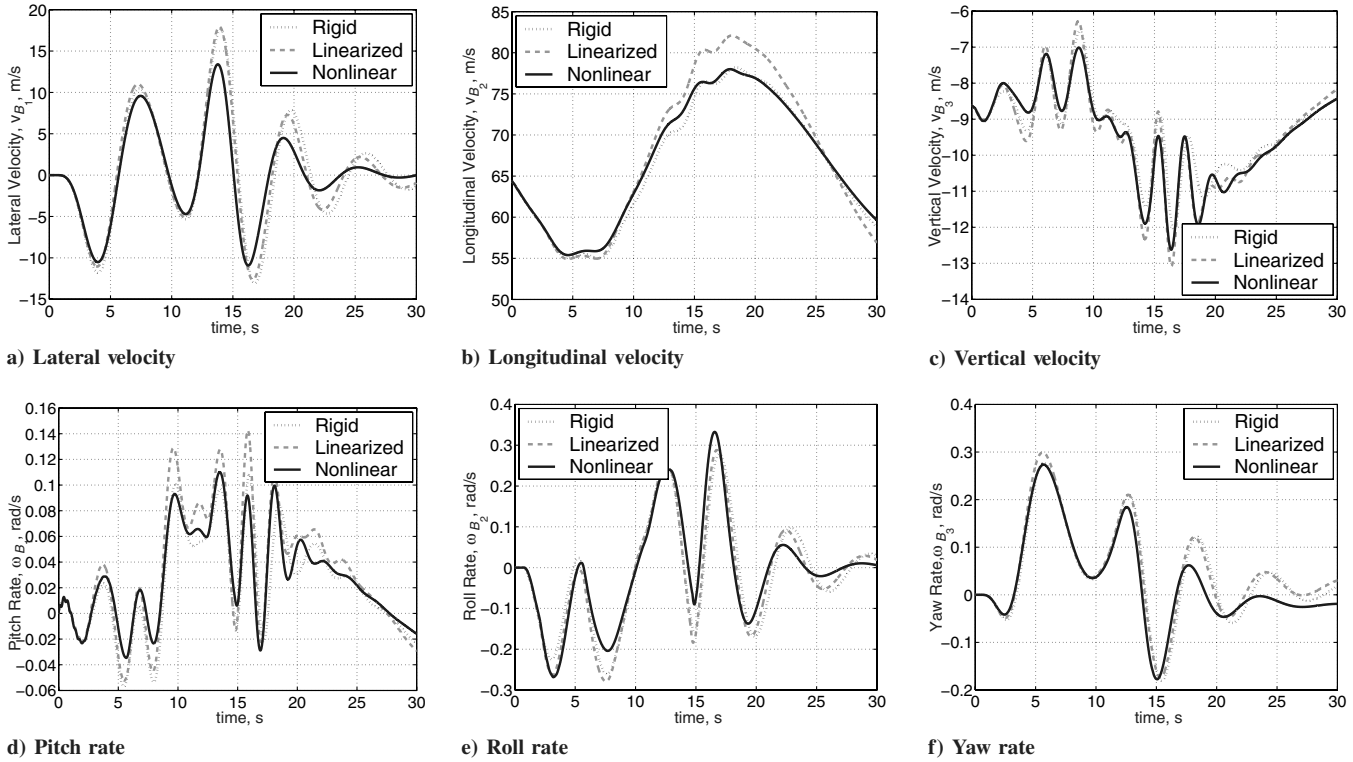

a) Lateral velocity **b) Longitudinal velocity** **c) Vertical velocity**

d) Pitch rate **e) Roll rate** **f) Yaw rate**

Fig. 16 *B* reference frame linear and angular rates; case 3, heavy.

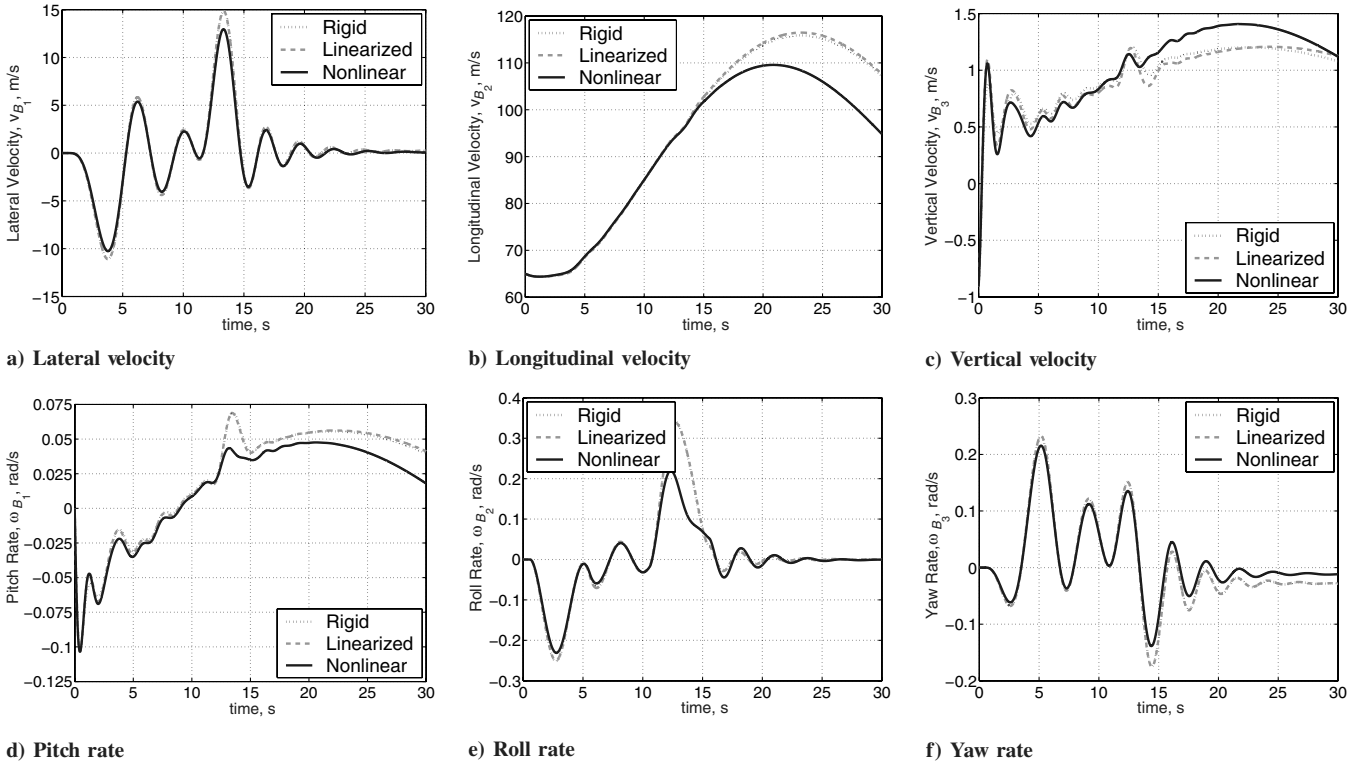

a) Lateral velocity b) Longitudinal velocity c) Vertical velocity

d) Pitch rate e) Roll rate f) Yaw rate

Fig. 17 *B* reference frame linear and angular rates; case 3, light.

motion of a reference point in the aircraft with the aeroelastic equations that govern its geometrically nonlinear structural response. The structural dynamic analysis of the entire vehicle used a low-order strain-based geometrically nonlinear formulation. The unsteady aerodynamics used an incompressible finite state potential-flow formulation. The coupled nonlinear flight dynamics/aeroelastic equations of motion were then integrated using an implicit modified Newmark method, incorporating first- and second-order nonlinear differential equations. Using the proposed framework, analyses and simulations were conducted in a representative twin-tailed HALE

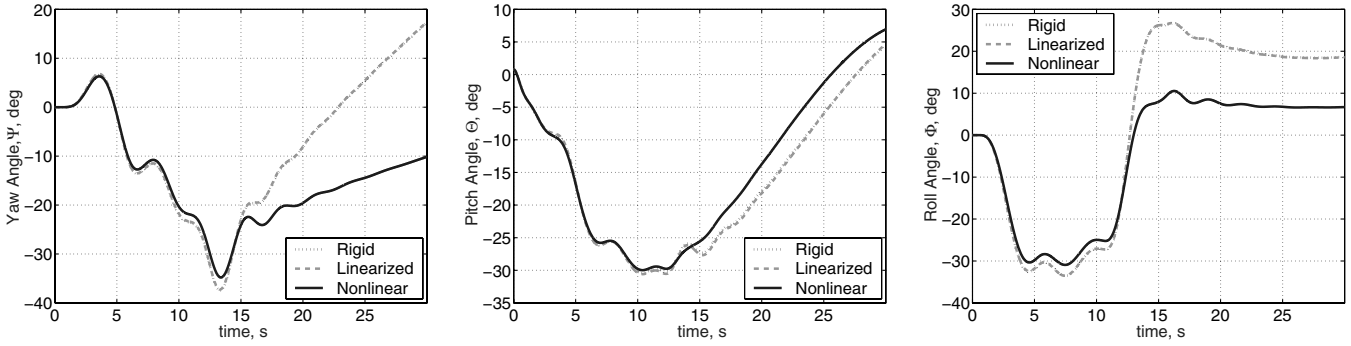

a) Yaw angle b) Pitch angle c) Roll angle

Fig. 18 *B* reference frame classic aircraft Euler angles; case 3, light.

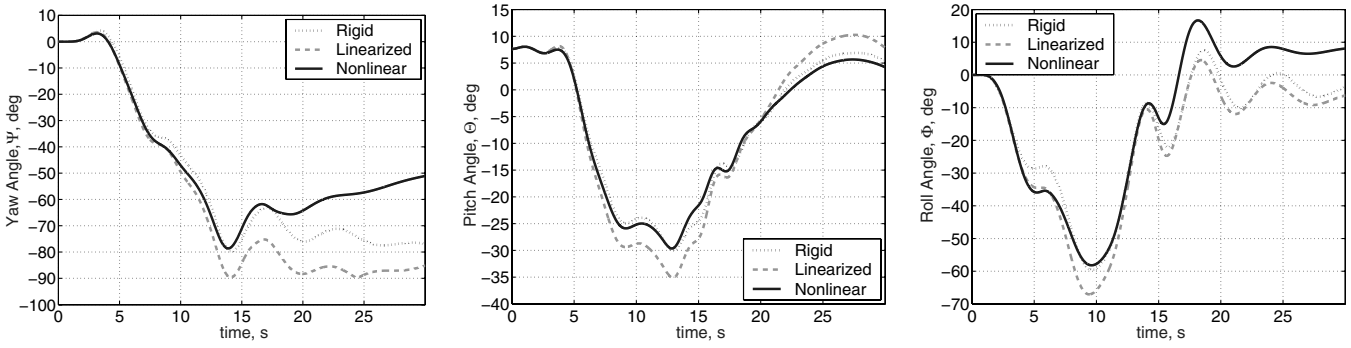

a) Yaw angle b) Pitch angle c) Roll angle

Fig. 19 *B* reference frame classic aircraft Euler angles; case 3, heavy.

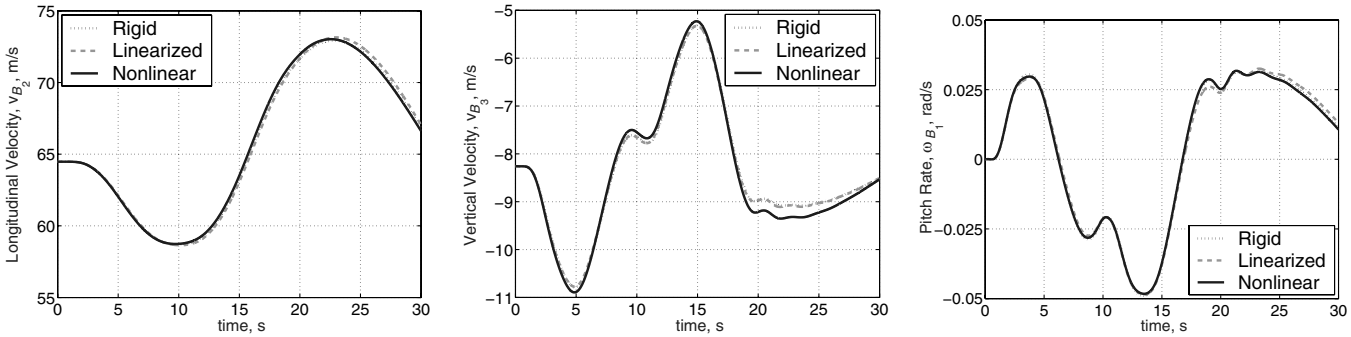

a) Longitudinal velocity b) Vertical velocity c) Pitch rate

Fig. 20 *B* reference frame relevant linear and angular rates; case 4, heavy.

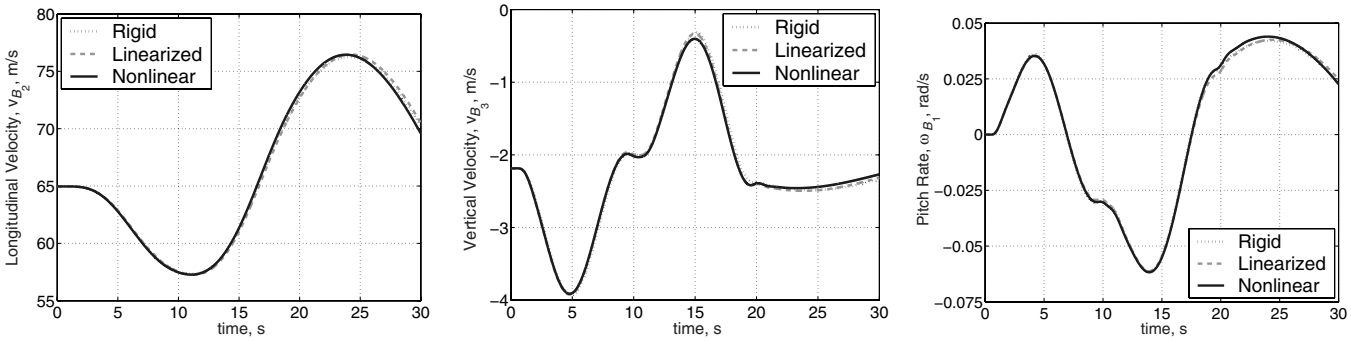

a) Longitudinal velocity b) Vertical velocity c) Pitch rate

Fig. 21 *B* reference frame relevant linear and angular rates; case 4, light.

vehicle. The investigated cases compared nonlinear rigid-body solutions, nonlinear vehicle 6-DOF coupled with the linearized aeroelastic solutions, and full nonlinear vehicle 6-DOF and aeroelastic solutions. Simulations used both full and empty fuel states for level gliding descent and powered level flight, low-pass square elevator input gliding descent, and low-pass-filtered square aileron input rolling/gliding descent. In all heavy weight cases, it was seen that the rigid-body solutions were not sufficient to capture the dynamics of a very flexible aircraft and higher-order formulations are required. When studying simple symmetric maneuvers, results indicated that linearized solutions may be acceptable to capture the main aircraft dynamics. However, when performing asymmetric maneuvering at heavy weight, results showed significant differences in the three reference point axes (pitch, roll, and yaw), requiring the

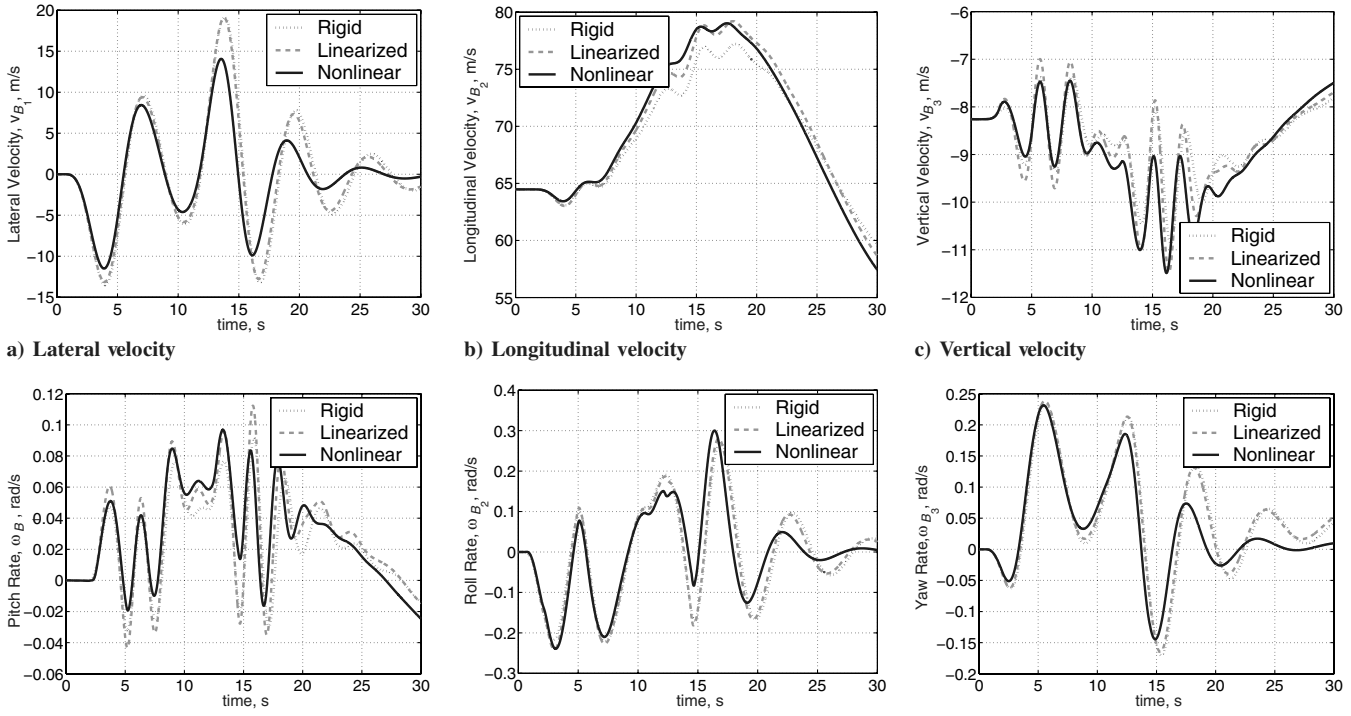

a) Lateral velocity b) Longitudinal velocity c) Vertical velocity

d) Pitch rate e) Roll rate f) Yaw rate

Fig. 22 *B* reference frame linear and angular rates; case 5, heavy.

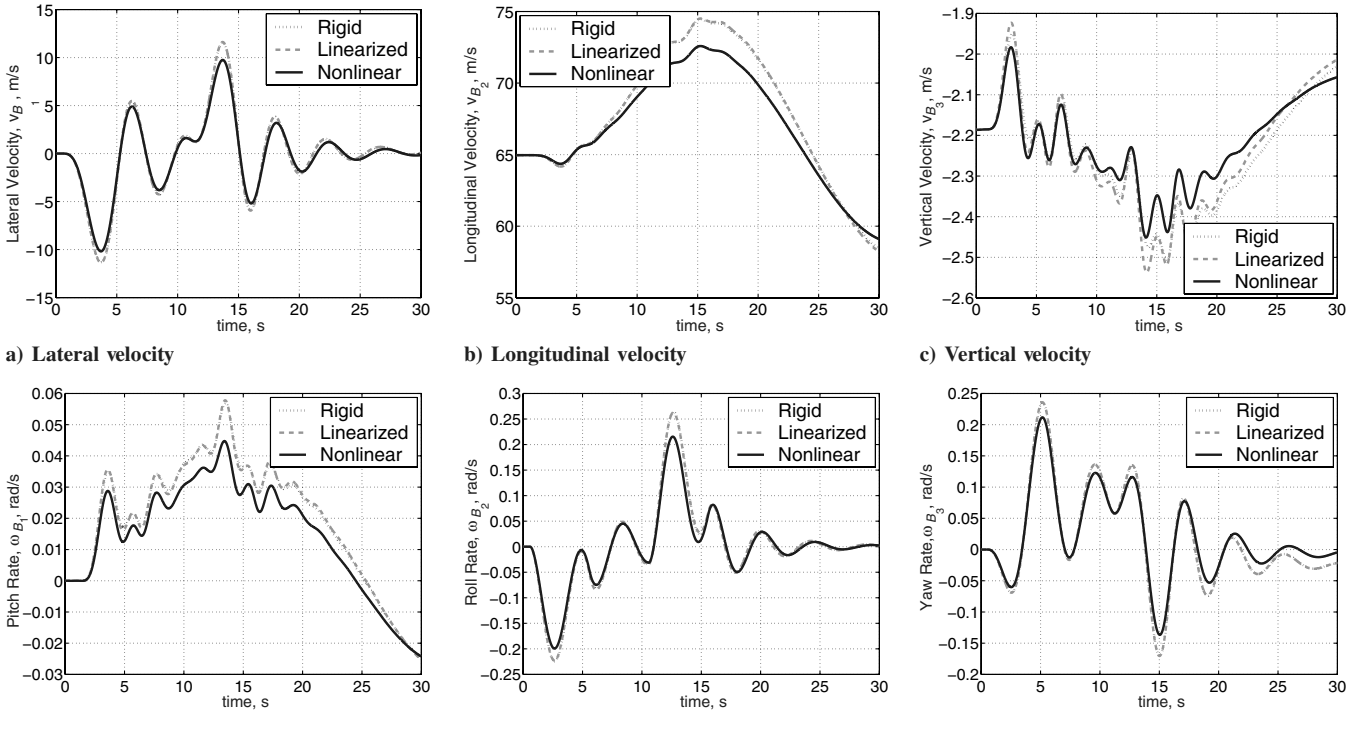

a) Lateral velocity **b) Longitudinal velocity** **c) Vertical velocity**

d) Pitch rate **e) Roll rate** **f) Yaw rate**

Fig. 23 *B* reference frame linear and angular rates; case 5, light.

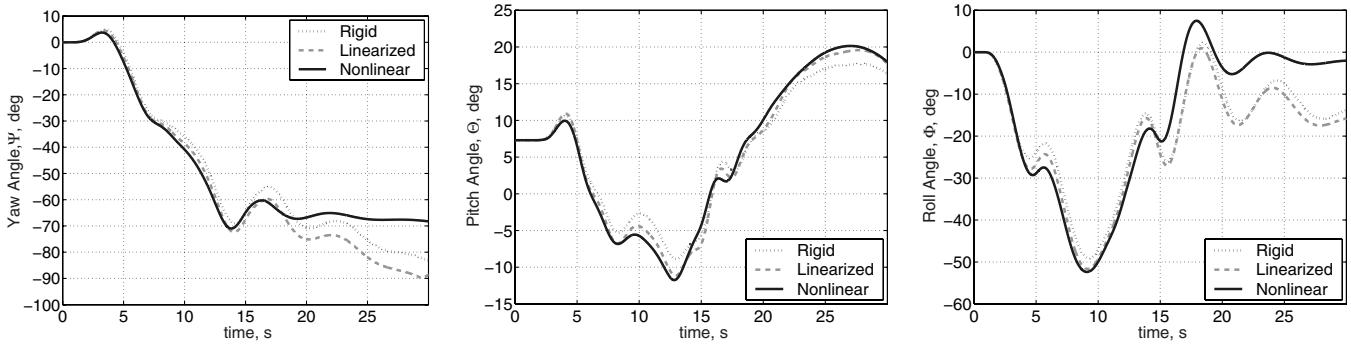

a) Yaw angle **b) Pitch angle** **c) Roll angle**

Fig. 24 *B* reference frame classic aircraft Euler angles; case 5, heavy.

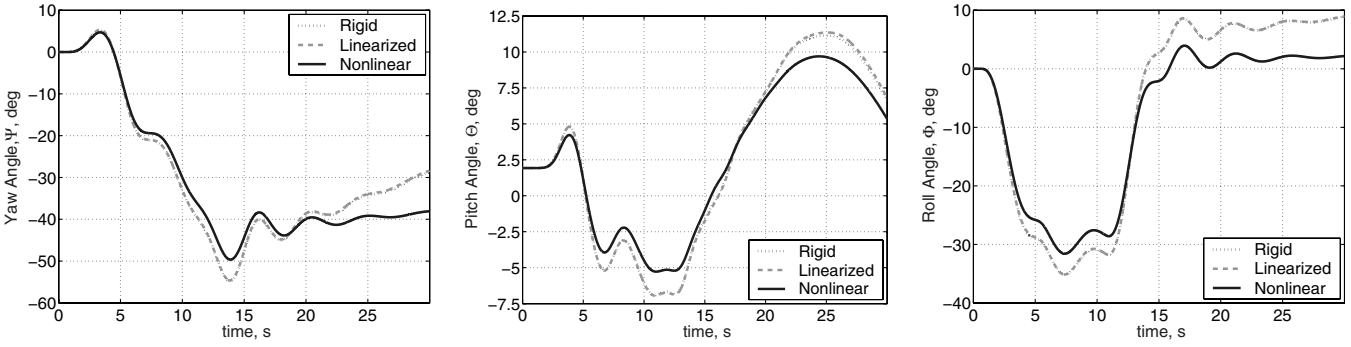

a) Yaw angle **b) Pitch angle** **c) Roll angle**

Fig. 25 *B* reference frame classic aircraft Euler angles; case 5, light.

nonlinear analysis approach to properly capture the vehicle response. Overall, simulation results showed the importance of having a minimum of a linearized structural analysis for symmetric maneuvering and nonlinear structural modeling for asymmetric maneuvering of a flexible aircraft such as those being considered for high-altitude long-endurance civilian and military missions.

Acknowledgments

This work was partially sponsored by AFOSR grant F49620-02-1-0425. The technical monitor was Clark Allred, U.S. Air Force. The views expressed in this article are those of the authors and do not reflect the official policy or position of the U.S. Air Force, U.S. Department of Defense, or the U.S. Government.

References

[1] Noll, T. E., Brown, J. M., Perez-Davis, M. E., Ishmael, S. D., Tiffany, G. C., and Gaier, M., "Investigation of the Helios Prototype Aircraft Mishap" [online article], http://www.nasa.gov/pdf/64317main_helios.pdf [retrieved 10 Feb. 2007]; also see NASA Press Release http://www.nasa.gov/home/hqnews/2004/sep/HQ_04283_helios_mishap.html.

[2] Tilmann, C. P., Flick, P. M., Martin, C. A., and Love, M. H., "High-Altitude Long Endurance Technologies for SensorCraft," Novel Vehicle Concepts and Emerging Vehicle Technologies Symposium, Brussels, Belgium, Applied Vehicle Technology Panel of NATO, Paper MP-104-P-26-1, 2003.

[3] Whitson, S., "The Proteus, Giving Shape to Forms Unknown," *Private Pilot*, Vol. 33, No. 12, Dec. 1998, pp. 44–50.

[4] Anon., "Unmanned Aircraft Systems Roadmap 2005–2030" [online report], Dept. of Defense, http://www.acq.osd.mil/usd/Roadmap%20Final2.pdf [retrieved 10 Feb. 2007].

[5] Friedmann, P. P., "Renaissance of Aeroelasticity and Its Future," *Journal of Aircraft*, Vol. 36, No. 1, Jan.–Feb. 1999, pp. 105–121.

[6] Livne, E., and Weisshaar, T. A., "Aeroelasticity of Nonconventional Airplane Configurations-Past and Future," *Journal of Aircraft*, Vol. 40, No. 6, Nov.–Dec. 2003, pp. 1047–1065.

[7] Livne, E., "Future of Airplane Aeroelasticity," *Journal of Aircraft*, Vol. 40, No. 6, Nov.–Dec. 2003, pp. 1066–1092.

[8] Schimdt, D. K., and Raney, D. L., "Modeling and Simulation of Flexible Flight Vehicles," AIAA Modeling and Simulation Technologies Conference and Exhibit, Boston, MA, AIAA Paper 98-4359, 1998.

[9] Pedro, J. O., and Bigg, C. G., "Development of a Flexible Embedded Aircraft/Control System Simulation Facility," AIAA Atmospheric Flight Mechanics Conference and Exhibit, San Francisco, CA, AIAA Paper 2005-5889, 2005.

[10] Reschke, C., "Flight Loads Analysis with Inertially Coupled Equations of Motion," AIAA Atmospheric Flight Mechanics Conference and Exhibit, San Francisco, CA, AIAA Paper 2005-6026, 2005.

[11] Kier, T. M., "Comparison of Unsteady Aerodynamic Modelling Methodologies with Tespect to Flight Loads Analysis," AIAA Atmospheric Flight Mechanics Conference and Exhibit, San Francisco, CA, AIAA Paper 2005-6027, 2005.

[12] Crimaldi, J. P., Britt, R. T., and Rodden, W. P., "Response of B-2 Aircraft to Nonuniform Spanwise Turbulence," *Journal of Aircraft*, Vol. 30, No. 5, Sept.–Oct. 1993, pp. 652–659.

[13] Van Schoor, M. C., and von Flotow, A. H., "Aeroelastic Characteristics of a Highly Flexible Aircraft," *Journal of Aircraft*, Vol. 27, No. 10, Oct. 1990, pp. 901–908.

[14] Patil, M. J., Hodges, D. H., and Cesnik, C. E. S., "Nonlinear Aeroelastic Analysis of Complete Aircraft in Subsonic Flow," *Journal of Aircraft*, Vol. 37, No. 5, Sept.–Oct. 2000, pp. 753–760.

[15] Goland, M., "The Flutter of a Uniform Cantilever Wing," *Journal of Applied Mechanics*, Vol. 12, No. 4, 1945, pp. A197–A208.

[16] Patil, M. J., Hodges, D. H., and Cesnik, C. E. S., "Nonlinear Aeroelasticity and Flight Dynamics of High-Altitude Long-Endurance Aircraft," *Journal of Aircraft*, Vol. 38, No. 1, Jan.–Feb. 2001, pp. 95–103; also AIAA Paper 99-1470, 1999.

[17] Drela, M., "Integrated Simulation Model for Preliminary Aerodynamic, Structural, and Control-Law Design of Aircraft," *40th AIAA/ASME/ASCE/AHS/ASC Structures, Structural Dynamics, and Materials Conference and Exhibit*, AIAA Reston, VA, 1999, pp. 1644–1656; also AIAA Paper 99-1394.

[18] Cesnik, C. E. S., and Brown, E. L., "Modeling of High Aspect Ratio Active Flexible Wings for Roll Control," Proceedings of the 43rd AIAA/ASME/ASCE/AHS Structures, Structural Dynamics, and Materials Conferences, Denver, CO, AIAA Paper 2002-1719, 2002.

[19] Cesnik, C. E. S., and Brown, E. L., "Active Wing Warping Control of a Joined-Wing Airplane Configuration," Proceedings of the 44th AIAA/ASME/ASCE/AHS Structures, Structural Dynamics, and Materials Conferences, Norfolk, VA, AIAA Paper 2003–1715, 2003.

[20] Brown, E. L., "Integrated Strain Actuation in Aircraft with Highly Flexible Composite Wings," Ph.D. Thesis, Massachusetts Inst. of Technology, Boston, MA, June 2003.

[21] Peters, D., and Johnson, M. J., "Finite-State Airloads for Deformable Airfoils on Fixed and Rotating Wings," *Aeroelasticity and Fluid/Structure Interaction*, American Society of Mechanical Engineers, New York, Nov. 1994, pp. 1–28.

[22] Peters, D. A., and Cao, W., "Finite State Induced Flow Models, Part 1: Two-Dimensional Thin Airfoil," *Journal of Aircraft*, Vol. 32, No. 2, Mar.–Apr. 1995, pp. 313–322.

[23] Cesnik, C. E. S., and Su, W., "Nonlinear Aeroelastic Modeling and Analysis of Fully Flexible Aircraft," 46th AIAA/ASME/ASCE/AHS/ASC Structures, Structural Dynamics and Materials Conference, Austin, TX, AIAA Paper 2005–2169, 2005.

[24] Patil, M. J., and Hodges, D. H., "Flight Dynamics of Highly Flexible Flying Wings," *Journal of Aircraft*, Vol. 43, No. 6, pp. 1790–1799, 2006.

[25] Su, W., and Cesnik, C. E. S., "Aeroelastic Response of Highly Flexible Flying Wings," 47th AIAA/ASME/ASCE/AHS/ASC Structures, Structural Dynamics, and Materials Conference and Exhibit, Newport, RI, AIAA Paper 2006-1636, May 2006.

[26] Patil, M. J., and Taylor, D. J., "Gust Response of Highly Flexible Aircraft," 47th AIAA/ASME/ASCE/AHS/ASC Structures, Structural Dynamics, and Materials Conference and Exhibit, Newport, RI, AIAA Paper 2006-1638, May 2006.

[27] Wang, Z., Chen, P. C., Liu, D. D., Mook, D. T., and Patil, M. J., "Time Domain Nonlinear Aeroelastic Analysis for HALE Wings," 47th AIAA/ASME/ASCE/AHS/ASC Structures, Structural Dynamics, and Materials Conference and Exhibit, Newport, RI, AIAA Paper 2006-1640, May 2006.

[28] Palacios, R., and Cesnik, C. E. S., "Static Nonlinear Aeroelasticity of Flexible Slender Wings in Compressible Flow," 46th AIAA/ASME/ASCE/AHS/ASC Structures, Structural Dynamics and Materials Conference, Austin, TX, AIAA Paper 2005-1945, 2005.

[29] Garcia, J. A., "Numerical Investigation of Nonlinear Aeroelastic Effects on Flexible High-Aspect-RatioWings," *Journal of Aircraft*, Vol. 42, No. 4, July–Aug. 2005, pp. 1025–1036.

[30] Blair, M., and Canfield, R. A., "A Joined-Wing Structural Weight Modeling Study," 43rd AIAA/ASME/ASCE/AHS/ASC Structures, Structural Dynamics, and Materials Conference, Denver, CO, AIAA Paper 2002-1337, Apr. 2002.

[31] Weisshaar, T. A., and Lee, D., "Aeroelastic Tailoring of Joined-Wing Configurations," 43rd AIAA/ASME/ASCE/AHS Structues, Structural Dynamics, and Materials Conference, Denver, CO, AIAA Paper 2002-1207, Apr. 2002.

[32] Tang, D., Conner, M. D., and Dowell, E. H., "Reduced-Order Aerodynamic Model and Its Application to a Nonlinear Aeroelastic System," *Journal of Aircraft*, Vol. 35, No. 2, Mar.–Apr. 1998, pp. 332–338.

[33] Tang, D., and Dowell, E. H., "Experimental and Theoretical Study on Aeroelastic Response of High-Aspect-Ratio Wings," *Journal of Aircraft*, Vol. 39, No. 8, Aug. 2001, pp. 1430–1441.

[34] Tang, D., and Dowell, E. H., "Experimental and Theoretical Study of Gust Response for High-Aspect-Ratio Wing," *Journal of Aircraft*, Vol. 40, No. 3, Mar. 2002, pp. 419–429.

[35] Dowell, E. H., and Tang, D., "Nonlinear Aeroelasticity and Unsteady Aerodynamics," *AIAA Journal*, Vol. 40, No. 9, Sept. 2002, pp. 1697–1707.

[36] Stevens, B. L., and Lewis, F. L., *Aircraft Control and Simulation*, Wiley, New York, 1992.

[37] Phillips, W. F., Hailey, C. E., and Gebert, G. A., "A Review of Attitude Kinematics for Aircraft Flight Simulation," AIAA Modeling and Simulation Technologies Conference and Exhibit, Denver, CO, AIAA Paper 2000-4302, 2000.

[38] Shearer, C. M., "Coupled Nonlinear Flight Dynamics, Aeroelasticity, and Control of Very Flexible Aircraft," Ph.D. Thesis, Univ. of Michigan, Ann Arbor, MI, 2006.

[39] Greenwood, D. T., *Advanced Dynamics*, Cambridge Univ. Press, Cambridge, England, U.K., 2003.

[40] Arora, J. S., *Introduction to Optimum Design*, McGraw–Hill, New York, 1989.

[41] Geradin, M., and Rixen, D., *Mechanical Vibrations: Theory and Applications to Structural Dynamics*, 2nd ed., Wiley, New York, May 1997.

[42] Jansen, K. E., Whiting, C. H., and Hulbert, G. M., "A Generalized-α Method for Integrating the Filtered Navier-Stokes Equations with a Stabilized Finite Element Method," *Computer Methods in Applied Mechanics and Engineering*, Vol. 190, Nos. 3–4, Oct. 2000, pp. 305–319.

[43] Chung, J., and Hulbert, G. M., "A Time Integration Algorithm for Structural Dynamics with Improved Numerical Dissipation: The Generalized-α Method," *Journal of Applied Mechanics*, Vol. 60, June 1993, pp. 371–375.

[44] Shearer, C. M., and Cesnik, C. E. S., "Modified Generalized-α Method for Integrating Governing Equations of Very Flexible Aircraft," 47th AIAA/ASME/ASCE/AHS/ASC Structures, Structural Dynamics, and Materials Conference, AIAA Paper 2006-1747, 2006.